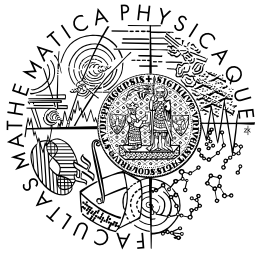

FACULTY
OF MATHEMATICS
AND PHYSICS
Charles University

ABSTRACT OF DOCTORAL THESIS

Tomáš Nosek

Study of Neutrino Oscillations at the NOvA Experiment

Institute of Particle and Nuclear Physics

Supervisor of the doctoral thesis:	RNDr. Karel Soustružník, Ph.D.
Study programme:	Physics
Study branch:	Particle and Nuclear Physics

Prague 2021

Disertační práce byla vypracována v rámci doktorského studia na Matematicko-fyzikální fakultě Univerzity Karlovy (MFF UK) v letech 2015–2021.

Autor:	Mgr. *et* Mgr. Tomáš Nosek
Obor studia:	P4F9 Částicová a jaderná fyzika
Školitel:	RNDr. Karel Soustružník, Ph.D.
Školící pracoviště:	Ústav částicové a jaderné fyziky Matematicko-fyzikální fakulta Univerzita Karlova *V Holešovičkách 2* *180 00 Praha 8, Česká republika*
Oponenti:	RNDr. Jaroslav Zálešák, Ph.D. Fyzikální ústav Akademie věd České republiky *Na Slovance 2* *182 21 Praha 8, Česká republika*
	RNDr. Ing. Bedřich Roskovec, Ph.D. Matematicko-fyzikální fakulta Univerzita Karlova *V Holešovičkách 2* *180 00 Praha 8, Česká republika*
Předseda oborové rady:	doc. RNDr. Karol Kampf, Ph.D. Matematicko-fyzikální fakulta Univerzita Karlova *V Holešovičkách 2* *180 00 Praha 8, Česká republika*

Obhajoba disertační práce se koná dne ..... v ..... hodin před komisí pro obhajoby disertačních prací v oboru P4F9 Částicová a jaderná fyzika na Ústavu částicové a jaderné fyziky MFF UK, V Holešovičkách 2, 180 00 Praha 8, v místnosti č. .....

S disertační prací je možno se seznámit na studijním oddělení pro doktorské studium MFF UK, Ke Karlovu 3, 121 16 Praha 2.

Contents

Introduction **1**

1 Neutrinos and neutrino oscillation phenomena **3**
1.1 Standard Model and neutrinos . . . 3
1.1.1 Neutrino masses . . . 3
1.1.2 Lepton mixing . . . 5
1.2 Mixing and oscillations in three neutrinos paradigm . . . 5
1.2.1 U_{PMNS} mixing matrix . . . 6
1.2.2 Neutrino oscillations in vacuum . . . 6
1.2.3 Neutrino oscillations in medium . . . 7
1.3 Status of neutrino oscillation parameters measurements . . . 7
1.4 Oscillation probabilities for long-baseline experiments . . . 8

2 The NOvA experiment **11**
2.1 Introduction and physics interests . . . 11
2.2 The NuMI beam . . . 11
2.3 Off-axis concept . . . 11
2.4 NOvA detectors . . . 12

3 The NOvA neutrino oscillation analysis **15**
3.1 Analysis strategy . . . 15
3.2 Improvements and changes in 2020 analysis . . . 15
3.3 Data sets . . . 16
3.4 NOvA simulations . . . 16
3.5 Event reconstruction . . . 16
3.6 Detectors energy calibration . . . 17
3.7 Particle identification algorithms . . . 18
3.7.1 Convolutional visual networks . . . 18
3.8 Energy estimation . . . 19
3.9 Event selection and analysis samples . . . 19
3.10 Near detector data constraints and decomposition . . . 21
3.11 Near to far extrapolation technique . . . 23
3.12 Unconstrained prediction components and cosmics . . . 24
3.13 Far detector predictions . . . 24

4 Systematic uncertainties **25**
4.1 Treatment of systematic uncertainties . . . 25
4.2 Summary and notes . . . 26

5 Results and constraints on neutrino oscillation parameters **27**
5.1 Best-fit estimates . . . 27
5.2 Far detector data . . . 27
5.3 Constraints on neutrino oscillation parameters . . . 28

Conclusion **35**

References **37**

List of publications **41**

Introduction

Neutrinos are likely the second most abundant of all known particles. There are at least three different neutrino types or "flavors" as identified in the charged current weak interactions: electron, muon, and tau (e, μ, τ). It is a well-established experimental fact that neutrino flavor is not conserved in space-time propagation, and the neutrino flavors "oscillate". A possible explanation requires neutrino (lepton) mixing and their non-vanishing mass. With the paramount evidence of neutrinos being massive, neutrino oscillation experiments are the foremost witnesses of the physics beyond the Standard Model, at the frontier of the human perception of the universe.

Neutrinos have been studied intensively for several decades. The simplest mixing model of three neutrino mass states in three interaction (flavor) states described by three mixing angles $(\theta_{12}, \theta_{23}, \theta_{13})$, a complex phase, and two differences of squared neutrino masses seems to be very well understood. However, there are still many questions whose answers are of utmost importance to finally provide a satisfactory theory of elementary particles.

NOvA is capable of investigating several of them: the size of mixing angle θ_{23} and squared mass-splitting Δm^2_{32}, CP symmetry and the size of δ_{CP}, *etc.* It is a long-baseline neutrino oscillation experiment and recently in operation. With its two detectors, it has been (for more than five years) looking for the disappearance of muon neutrinos and the appearance of electron neutrinos of $\sim$GeV energies in (as of yet) the most powerful muon neutrino beam over an 810 km distance (long-baseline).

This thesis intends to depict the NOvA neutrino oscillation analysis within the minimal model of three massive neutrinos in the latest state of the art (Jun 2020).

The text is organized into five subsequent chapters. Chapter 1 reviews the neutrino oscillation *status quo*, Chapter 2 is an informative overview of the NOvA experiment, Chapter 3 unveils the NOvA neutrino oscillation analysis within the three neutrinos model, Chapter 4 surveys all the considered systematic uncertainties, and Chapter 5 shows the results, and it reports the estimates on the neutrino oscillation parameters.

The system of natural units ("Planck units") is used throughout the text, $c = \hbar = k_{\mathrm{B}} = 1$, and the CPT theorem is assumed to be valid unless stated otherwise.

1. Neutrinos and neutrino oscillation phenomena

The first chapter presents the broader theoretical context of neutrinos as genuine objects of particle physics and reveals the immediate phenomenological milieu of neutrino oscillations.

1.1 Standard Model and neutrinos

Neutrinos belong to the set of currently considered "elementary particles", *i.e.* fundamental physical objects with unrecognized substructure or intrinsic constituents. Elementary particles and their interactions, except for gravity, are well described by the Standard Model (SM) of particle physics (*e.g.*, see Ref. [1]).

The complete set of the SM elementary particles, their properties, interactions, and relations are illustrated by Fig. 1.1. By the topic of this thesis and this section, the following text focuses on the neutrinos and their features only, *i.e.* lepton mixing, neutrino oscillations, and neutrino masses.

Each massive and charged elementary particle of the SM has an antiparticle partner with opposite additive quantum numbers and identical dynamical quantum numbers. The operator of charge conjugation C transforms one into another. In this sense, all neutral bosons are their own antiparticles, and the term "antiparticle" does not have a clear interpretation for them. Since neutrinos are also neutral, it might be they are, in contrast to other fermions, their own antiparticles too. That would allow total lepton number violating processes (*e.g.* neutrinoless double β-decay, see Ref. [2, Chapter 8]), and this type of neutrinos are described as Majorana particles in theory. Still, no such processes have been observed yet [3]. There is an omnipresent ambiguity whether neutrinos shall be described as pure Dirac-like particles or Majorana particles – see, *e.g.*, Ref. [2].

1.1.1 Neutrino masses

Dictated by the observation of neutrino flavor transitions and their presumable implication of non-zero neutrino masses, the SM of massless neutrinos has to be properly extended. Relevant mass terms need to be introduced into the SM Lagrangian, which coincidentally always require new SM objects (at least one right-handed ν_R field), *e.g.*, see Ref. [4].

The easiest way is to add the corresponding ν_R to the existing ν_L. They would combine into the so-called Dirac mass terms of the form $\bar{\nu}_L\nu_R + \bar{\nu}_R\nu_L$ similarly to other fermions in the SM [4, Chapter 6]. In fact, these Dirac masses can be seen as a special solution to a general Majorana case (see Ref. [5, p. 27]). With the Dirac (D) and Majorana "left-handed" (M_L) and "right-handed" (M_R) mass constants, there are three types of neutrino mass terms in the SM-like Lagrangian in the flavor basis: Dirac $\bar{\nu}_L D\nu_R$ (+h.c.) and two Majorana terms $\bar{\nu}_L M_L \nu_L^C$ and $\bar{\nu}_R^C M_R \nu_R$ (+h.c.) with ν^C being the charge conjugated field $\nu^C \equiv C\bar{\nu}^\top$.

The Dirac mass terms could be associated with Yukawa interaction after spontaneous EW symmetry breaking in correspondence to the charged fermions [2, p. 57]. The Majorana mass terms break the lepton number by 2 (two neutrino fields). However, they are allowed only if neutrinos are truly neutral. The fields have to satisfy the Majorana condition of "particle ≡ antiparticle" [4].

In the basis of n neutrino mass eigenstates ν_i^{M} with masses m_i, the mass terms have the form $m_i\bar{\nu}_i^{\mathrm{M}}\nu_i^{\mathrm{M}}$. Here, $\nu^{\mathrm{M}} = \nu + \nu^C, \nu^{\mathrm{M}} = (\nu^{\mathrm{M}})^C$ are Majorana neutrino fields, for they manifestly obey the Majorana condition, and Majorana neutrinos are described by only one two-component field.

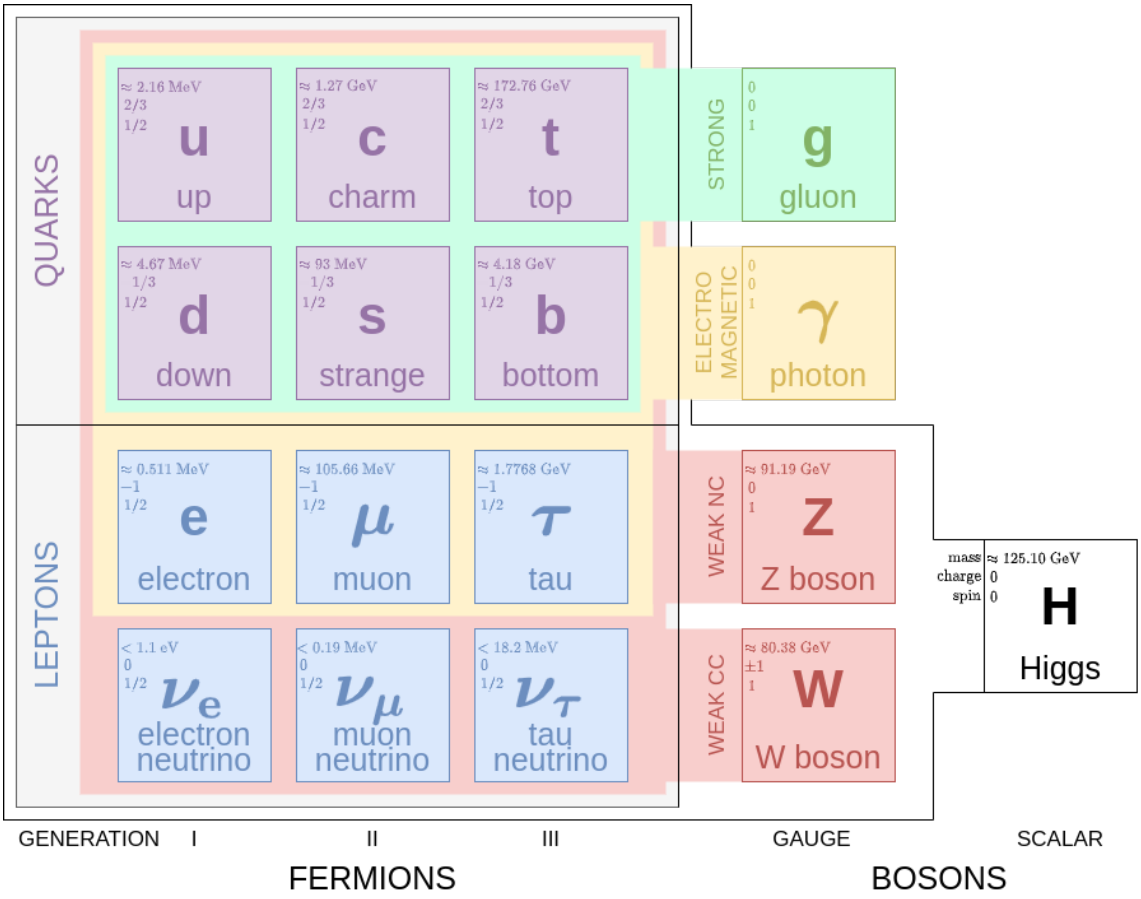

Figure 1.1: Diagram illustrating the elementary particles of the SM and their properties. The left part shows three generations of elementary fermions. Each consists of a pair (left-handed weak flavor doublet) of quarks (upper, purple) and a pair of leptons (lower, blue) to illustrate the corresponding doublets for left-handed chiral fields. Right-handed fields are singlets with vanishing coupling constants in the case of neutrinos. The right part shows the bosons of the SM, gauge bosons together with couplings to fermions: strong interaction in green, electromagnetic in yellow, and weak CC and NC in red. One scalar Higgs boson responsible for the generation of masses of fermions, $W^{\pm}$, and Z is in white. The stated masses are taken from Ref. [3].

The relations between ν^{M} and the active weak flavors $\nu_{\alpha L}$ can be retrieved as [3]

$$\nu_{\alpha L} = P_L \sum_{i}^{n} V_{\alpha i} \nu_i^{\mathrm{M}}, \tag{1.1}$$

where P_L is the left projector, $V_{\alpha i}$ are elements of a matrix V to diagonalize the original mass matrix in the flavor basis, and $\alpha = e, \mu$, or τ of the weak active flavors.

Specific constrictions to this general approach lead to the well-known "See-Saw" mechanism to reclaim a spectrum of the three SM light neutrinos and several heavy neutrinos. This See-Saw type I is formulated, *e.g.*, in Ref. [2].

1. Assume there are no left-handed Majorana mass terms, *i.e.*, $M_L = 0$.

2. Assume the Dirac mass terms are generated by the SM Higgs mechanism.

3. Assume the lepton number conservation is violated at a much larger scale than the EW

scale, *i.e.*, the eigenvalues of M_R are much larger than the vacuum expectation of the Higgs field (the Dirac masses), formally denoted as $M_R \gg D$.

Then, there is a spectrum of lighter neutrinos with masses proportional to $D^\top M_R^{-1} D$ (three observed neutrinos) and very heavy neutrinos with masses proportional to M_R. The See-Saw mechanism is one of the simplest theoretical extensions for which the SM might be considered a good effective low energy model.

1.1.2 Lepton mixing

With n neutrino mass eigenstates denoted ν_i, $\nu_1, \nu_2, \nu_3, \ldots, \nu_n$, $n \geq 3$, and three active lepton flavors $\alpha = e, \mu, \tau$, the SM interaction Lagrangian $\mathcal{L}^{(\mathrm{CC})}_{\mathrm{int,lep}}$ can be written as [4]

$$\mathcal{L}^{(\mathrm{CC})}_{\mathrm{int,lep}} = -\frac{g}{2\sqrt{2}} \sum_{\alpha,i} \bar{l}_\alpha \gamma^\lambda (1-\gamma_5) U_{\alpha i} \nu_i W^-_\lambda + \mathrm{h.c.}, \tag{1.2}$$

where U is a $3 \times n$ complex matrix. $U_{\alpha i}$ are immediately identified as the corresponding $V_{\alpha i}$.

A $3 \times n$ complex matrix has $6n$ real parameters. The $UU^\dagger = \mathbb{1}_{3\times 3}$ represents nine independent real conditions, *i.e.*, $3(2n-3)$ parameters are independent, out of which $3(n-2)$ parameters are rotational angles, and the rest are phases. Three of $3(n-1)$ phases are physically irrelevant, for they can be arbitrarily fixed by phase redefinition of the three charged lepton fields l_α. Moreover, for degenerate neutrino mass states, the number of relevant phases is further reduced by up to $n-1$ for pure Dirac neutrinos in general [5]. In conclusion, for $n \geq 3$, there are $3(n-2)$ physically independent rotational angles and $3(n-2)$ phases ($2n-5$ for Dirac neutrinos).

1.2 Mixing and oscillations in three neutrinos paradigm

In the sense of Occam's razor, the minimal three neutrinos spectrum is an effective or even exact model for several possibly realized scenarios (using the notation from Subsection 1.1.1):

- There are only three Dirac neutrinos with tiny masses, $n = 3$, $M_L = M_R = 0$.
- There are only three pure Majorana mass states (as noted, this scenario would still require a revision of the SM and its content).
- (See-Saw) There are three light active neutrinos and a number of heavy sterile neutrinos, *i.e.*, $M_L = 0, M_R \gg D$. Then, U cannot be unitary. However, the "violation" of the unitary conditions would be of the order (formally) $\mathcal{O}(D/M_R)$.
- Solutions similar to the previous point of a mass spectrum with three isolated neutrinos, where the rest have masses at much different scales, could manifest as an effective three neutrinos mixing with small unitarity violation.

Throughout the text from now on, the three neutrinos paradigm (3ν-paradigm) is used in its standard formulation. The three active neutrino flavors are identified, by definition, in weak CC interactions with the corresponding charged leptons ($e \leftrightarrow \nu_e$, $\mu \leftrightarrow \nu_\mu$, $\tau \leftrightarrow \nu_\tau$). This flavor representation $\boldsymbol{\nu}_f \equiv (\nu_e, \nu_\mu, \nu_\tau)^\top$ is related to the neutrino mass representation $\boldsymbol{\nu}_m \equiv (\nu_1, \nu_2, \nu_3)^\top$ as

$$\boldsymbol{\nu}_f = U \boldsymbol{\nu}_m, \tag{1.3}$$

or in terms of the neutrino quantum states (flavor and mass eigenstates):

$$|\nu_i\rangle = \sum_\alpha U_{\alpha i} |\nu_\alpha\rangle, \qquad |\nu_\alpha\rangle = \sum_i U^*_{\alpha i} |\nu_i\rangle, \qquad (\alpha = e, \mu, \tau; \quad i = 1, 2, 3), \tag{1.4}$$

where $U_{\alpha i}$ are the elements of U. The three neutrino mass eigenstates $|\nu_i\rangle$ have well-defined masses m_i, and they are assumed to be orthonormal (with Kronecker δ):

$$\langle \nu_i | \nu_j \rangle = \delta_{ij}. \tag{1.5}$$

1.2.1 U_{PMNS} mixing matrix

In the 3ν-paradigm, U has up to six independent parameters. It is parametrized with three mixing angles θ_{ij}, a complex phase δ_{CP}, and two Majorana phases a, b as a product of three rotational matrices $U_{ij}(\theta_{ij})$, $I_{\delta_{\text{CP}}} \equiv \text{diag}(1, 1, \exp(\text{i}\delta_{\text{CP}}))$, and $I_A \equiv \text{diag}(\exp(\text{i}a/2), \exp(\text{i}b/2), 1)$. With $\text{c}_{ij}, \text{s}_{ij} \equiv \cos\theta_{ij}, \sin\theta_{ij}$, this can be written as [4, 2, 5, 6, 3]

$$U = \begin{pmatrix} U_{e1} & U_{e2} & U_{e3} \\ U_{\mu 1} & U_{\mu 2} & U_{\mu 3} \\ U_{\tau 1} & U_{\tau 2} & U_{\tau 3} \end{pmatrix} = U_{23}(\theta_{23}) I_{\delta_{\text{CP}}} U_{13}(\theta_{13}) I^*_{\delta_{\text{CP}}} U_{12}(\theta_{12}) I_A =$$

$$= \begin{pmatrix} 1 & & \\ & c_{23} & s_{23} \\ & -s_{23} & c_{23} \end{pmatrix} \begin{pmatrix} c_{13} & & s_{13}\text{e}^{-\text{i}\delta_{\text{CP}}} \\ & 1 & \\ -s_{13}\text{e}^{+\text{i}\delta_{\text{CP}}} & & c_{13} \end{pmatrix} \begin{pmatrix} c_{12} & s_{12} & \\ -s_{12} & c_{12} & \\ & & 1 \end{pmatrix} \begin{pmatrix} \text{e}^{\text{i}\frac{a}{2}} & & \\ & \text{e}^{\text{i}\frac{b}{2}} & \\ & & 1 \end{pmatrix} =$$

$$= \begin{pmatrix} c_{13}c_{12} & c_{13}s_{12} & s_{13}\text{e}^{-\text{i}\delta_{\text{CP}}} \\ -c_{23}s_{12} - s_{13}c_{12}s_{23}\text{e}^{+\text{i}\delta_{\text{CP}}} & c_{23}c_{12} - s_{13}s_{12}s_{23}\text{e}^{+\text{i}\delta_{\text{CP}}} & c_{13}s_{23} \\ s_{23}s_{12} - s_{13}c_{12}c_{23}\text{e}^{+\text{i}\delta_{\text{CP}}} & -s_{23}c_{12} - s_{13}s_{12}c_{23}\text{e}^{+\text{i}\delta_{\text{CP}}} & c_{13}c_{23} \end{pmatrix} \times \begin{pmatrix} \text{e}^{\text{i}\frac{a}{2}} & & \\ & \text{e}^{\text{i}\frac{b}{2}} & \\ & & 1 \end{pmatrix}, \tag{1.6}$$

where $\theta_{ij} \in [0, \pi/2]$ and $\delta_{\text{CP}}, a, b \in [0, 2\pi]$. If neutrinos are Dirac-like particles, there is effectively only one complex phase, δ_{CP}, and the neutrino mixing matrix U is usually referred to as the Pontecorvo-Maki-Nakagawa-Sakata (PMNS, U_{PMNS}) mixing matrix.

1.2.2 Neutrino oscillations in vacuum

Lepton flavor violation in neutrino propagation is a prompt consequence of the neutrino mixing leading to neutrino flavor oscillations as a function of space-time coordinates.

A neutrino of energy E produced in a source through a weak CC interaction with a charged lepton l_α travels to a distance L, where it undergoes another CC interaction with a charged lepton l_β. *Ipso facto*, the neutrino is born as ν_α and transforms into ν_β, Fig. 1.2.

With the prevalent assumption that $|\nu\rangle$ is a plane wave [7], it is straightforward to compute the probability of the this $\nu_\alpha \to \nu_\beta$ transition [4, 5, 8, 7]:

$$\begin{aligned} P(\nu_\alpha \to \nu_\beta; L, E) = \delta_{\alpha\beta} \quad &- \quad 4 \sum_{i>j} \mathfrak{Re}(U^*_{\alpha i} U_{\alpha j} U_{\beta i} U^*_{\beta j}) \sin^2\left(\frac{\Delta m^2_{ij}}{4E} L\right) + \\ &+ \quad 2 \sum_{i>j} \mathfrak{Im}(U^*_{\alpha i} U_{\alpha j} U_{\beta i} U^*_{\beta j}) \sin\left(\frac{\Delta m^2_{ij}}{2E} L\right), \end{aligned} \tag{1.7}$$

where Δm^2_{ij} are the differences of squared neutrino masses

$$\Delta m^2_{ij} = m^2_i - m^2_j. \tag{1.8}$$

From Eq. (1.7), if corresponding elements of U and Δm^2_{ij} are non-zero, $P(\nu_\alpha \to \nu_\beta; L, E)$ has oscillatory patterns. It is a function of L (or L/E in general) with oscillation lengths

$$L^{\text{osc}}_{ij} = \frac{4\pi E}{|\Delta m^2_{ij}|} \tag{1.9}$$

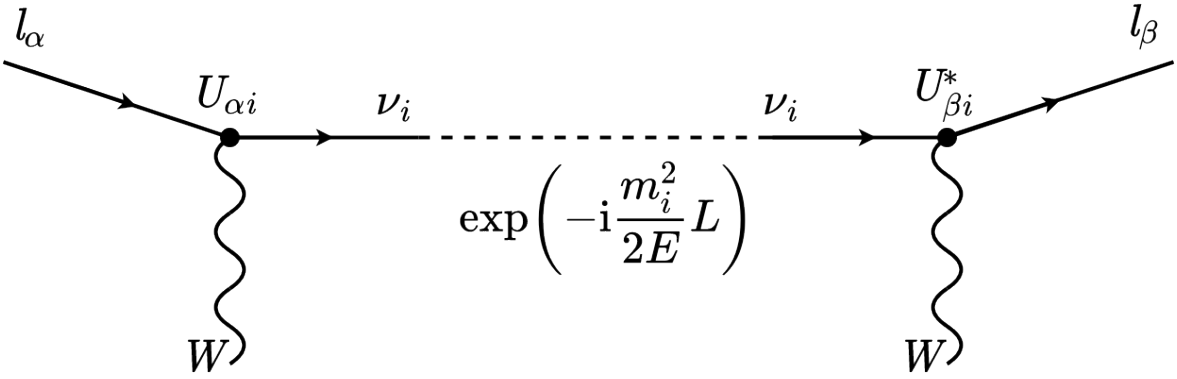

Figure 1.2: Feynmann-like diagram of a ν_i contribution to the $\nu_\alpha \to \nu_\beta$ flavor transition.

and amplitudes proportional to the mixing parameters θ_{ij} and δ_{CP}. This phenomenon is known as "neutrino oscillations".

To obtain equivalent oscillation probabilities to Eq. (1.7) for antineutrinos, one can employ the CPT theorem or replace $U \to U^*$:

$$P(\bar{\nu}_\alpha \to \bar{\nu}_\beta; L, E) = P(\nu_\beta \to \nu_\alpha; L, E). \tag{1.10}$$

If the 3ν-paradigm provides a complete description of neutrino mixing, U is unitary, $\langle \nu_\alpha | \nu_\beta \rangle = \delta_{\alpha\beta}$, and

$$\sum_{\beta=e,\mu,\tau} P(\nu_\alpha \to \nu_\beta; L, E) = 1 = \sum_{\beta=e,\mu,\tau} P(\nu_\beta \to \nu_\alpha; L, E). \tag{1.11}$$

Summarizing, neutrino flavor transitions in the 3ν-paradigm have oscillatory patterns that are fully described by six physical parameters: three lepton mixing angles θ_{12}, θ_{13}, and θ_{23}, one CP-violating mixing phase δ_{CP}, and two independent squared mass differences Δm^2_{21} and Δm^2_{32}.

1.2.3 Neutrino oscillations in medium

When propagating in a medium, neutrinos can interact with its constituents through weak coherent forward scattering illustrated by Fig. 1.3. The medium remains unchanged in coherent interactions. That allows for the interference of the forward scattered and unscattered neutrinos affecting the phase velocity of the neutrino wave, *i.e.*, neutrinos have different effective masses in matter from those in vacuum. They can be expressed in terms of effective potentials of particular scattering processes, which are proportional to the Fermi coupling constant G_{F} and densities of the scattering targets.

The potentials contribute to the neutrino propagation Hamiltonian, which needs to be diagonalized to identify the propagation basis and to calculate $P(\nu_\alpha \to \nu_\beta)$. This represents an *a posteriori* understanding of matter effects in neutrino oscillations in the sense that the evolution of a neutrino state is described relative to the medium properties at particular spatial coordinates x.

There is a vast theoretical and phenomenological background to the neutrino oscillations in matter. For more information on this topic in general, please discuss Refs. [9, 10, 11].

1.3 Status of neutrino oscillation parameters measurements

There have been many direct and indirect observations of neutrino flavor transitions supporting the original hypothesis of neutrino mixing and their non-vanishing mass. A global

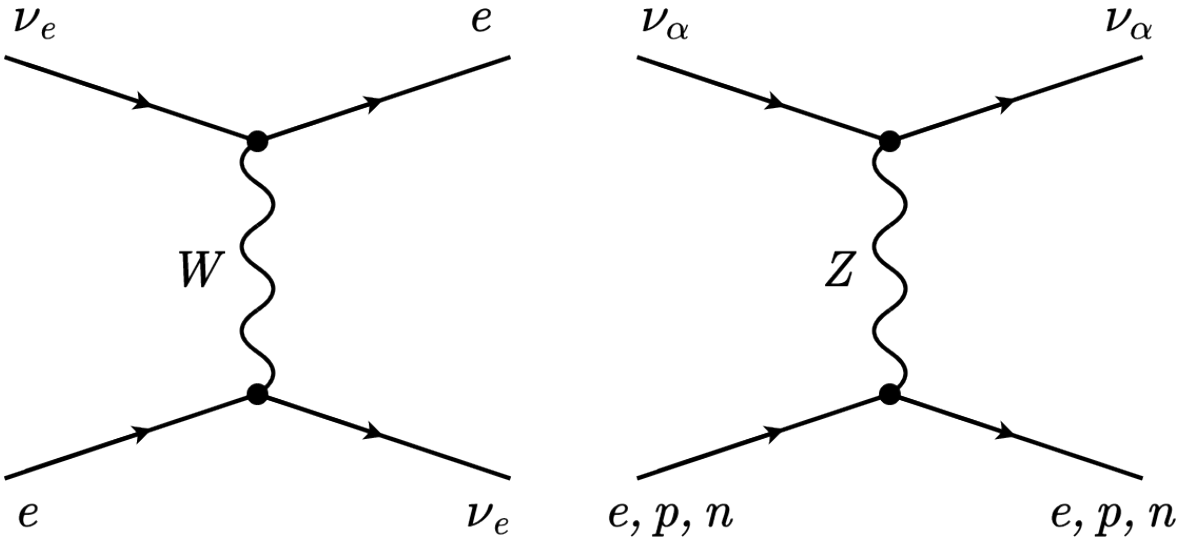

Figure 1.3: Feynmann diagrams of neutrino weak interactions in medium of CC forward scattering on e mediated by W (left) and NC scattering mediated by Z (right).

analysis of solar, atmospheric, accelerator, and reactor neutrino oscillation data within the 3ν-paradigm is provided by the NuFIT[1] group in Ref. [12], see Table 1.1.

There are two oscillation scales of $\Delta m^2_{21} \approx 7.5 \times 10^{-5}\,\text{eV}^2$ and $|\Delta m^2_{32(1)}| \approx 2.5 \times 10^{-3}\,\text{eV}^2$, with $\Delta m^2_{21}/|\Delta m^2_{32(1)}| \approx 0.03$. The sign of the larger squared mass splitting $\Delta m^2_{32(1)}$ remains unknown, which leaves two options designated as

1. **Normal ordering** (NO, or "normal hierarchy", NH) of the masses of neutrino mass eigenstates for $\Delta m^2_{32} > 0\ \text{eV}^2$, *i.e.*, $m^2_3 \gg m^2_2 > m^2_1$, and

2. **Inverted ordering** (IO, or "inverted hierarchy", IH) of the masses of neutrino mass eigenstates for $\Delta m^2_{32} < 0\ \text{eV}^2$, *i.e.*, $m^2_2 > m^2_1 \gg m^2_3$.

Secondly, two of three mixing angles are determined with good precisions: $\sin^2\theta_{12} \approx 0.3$ and $\sin^2\theta_{13} \approx 0.022$. On the other hand, there is an interesting ambiguity in the allowed $\sin^2\theta_{23}$ value as it is very close to the symmetric maximal possible 23 mixing $\theta_{23} = 45°$.

Finally, though the recent measurements from T2K [13, 14] suggest $\delta_{\text{CP}} \approx 3\pi/2$ close to the maximal *CP* violation in neutrino oscillations, the direct single-experiment measurements of δ_{CP} cannot pinpoint its value precisely enough to reject $\delta_{\text{CP}} = 0, \pi$ (no *CP* violation) at sufficient confidence levels ($<3\sigma$).

1.4 Oscillation probabilities for long-baseline experiments

The accelerator long-baseline experiments (currently operational NOvA, T2K, future DUNE) measure neutrino oscillation parameters in the $\nu_\mu \to \nu_\mu$ and $\nu_\mu \to \nu_e$ (or ν_τ) channels with ν_μ beams traveling through the Earth's crust. In the 3ν-paradigm, the relevant probabilities are expressed as expansions in two small parameters $\sin\theta_{13}$ and $\varepsilon \equiv \Delta m^2_{21}/\Delta m^2_{32}$ [16].

Using $c_{ij}, s_{ij} \equiv \cos\theta_{ij}, \sin\theta_{ij}$,

$$P(\nu_\mu \to \nu_\mu; L, E) \approx 1 - c^2_{13}\sin^2(2\theta_{23})\sin^2\frac{\Delta m^2_{32}L}{4E} + \mathcal{O}(\varepsilon, s^2_{13}). \tag{1.12}$$

[1] http://www.nu-fit.org (as of Mar 2021)

Table 1.1: Current status (Aug 2020) of the neutrino oscillation parameters estimates within the 3ν-paradigm as presented by the NuFIT group [12]. The estimates are reported under two different hypotheses of the neutrino mass ordering (hierarchy): normal (NO) $\Delta m^2_{3l} \equiv \Delta m^2_{31} > 0$ eV^2 (left) and inverted (IO) $\Delta m^2_{3l} \equiv \Delta m^2_{32} < 0$ eV^2 (right). The best fit of the NuFIT analysis is for NO.

	Normal ordering (best fit)		Inverted ordering	
	Best fit $\pm 1\sigma$	3σ range	Best fit $\pm 1\sigma$	3σ range
$\sin^2\theta_{12}$	0.304 ± 0.012	$0.269 - 0.343$	$0.304^{+0.013}_{-0.012}$	$0.269 - 0.343$
$\sin^2\theta_{23}$	$0.573^{+0.016}_{-0.020}$	$0.415 - 0.616$	$0.575^{+0.016}_{-0.019}$	$0.419 - 0.617$
$\sin^2\theta_{13}$	$0.02219^{+0.00062}_{-0.00063}$	$0.02032 - 0.02410$	$0.02238^{+0.00063}_{-0.00062}$	$0.02052 - 0.02428$
$\frac{\Delta m^2_{21}}{10^{-5}\text{ eV}^2}$	$7.42^{+0.21}_{-0.20}$	$6.82 - 8.04$	$7.42^{+0.21}_{-0.20}$	$6.82 - 8.04$
$\frac{\Delta m^2_{3l}}{10^{-3}\text{ eV}^2}$	$2.517^{+0.026}_{-0.028}$	$2.435 - 2.598$	-2.498 ± 0.028	$-2.581 - -2.414$
$\frac{\delta_{\rm CP}}{\pi}$	$1.09^{+0.15}_{-0.13}$	$0.67 - 2.05$	$1.57^{+0.14}_{-0.17}$	$1.07 - 1.96$

Assuming a constant matter density in the Earth's crust $N_e(x) = N_e = 6.4$ (10.3) keV^3, $\nu_\mu \to \nu_e$ oscillation probability is

$$P(\nu_\mu \to \nu_e; L, E, A) \approx 4 s^2_{13} s^2_{23} \frac{\sin^2\Delta}{(1-A)^2} + \varepsilon^2 \sin^2 2\theta_{12} c^2_{23} \frac{\sin^2 A\Delta}{A^2} + \\ + 8\, \varepsilon\, c_{12} s_{12} c_{23} s_{23} c^2_{13} s_{13} \cos(\Delta + \delta_{\rm CP}) \frac{\sin A\Delta}{A} \frac{\sin\Delta(1-A)}{1-A}, \qquad (1.13)$$

where

$$\Delta \equiv \frac{\Delta m^2_{31} L}{4E}, \qquad A \equiv \sqrt{2} G_{\rm F} N_e \frac{2E}{\Delta m^2_{31}}. \qquad (1.14)$$

The ν_e appearance Eq. (1.13) is sensitive to $\delta_{\rm CP}$, *i.e.* to the CP violation in oscillations, and through ε, Δ and A also to the sign of $\Delta m^2_{32(1)}$, *i.e.* the neutrino mass ordering. The probabilities for antineutrinos are formally obtained by $A \to -A$ and $\delta_{\rm CP} \to -\delta_{\rm CP}$ in the formulae above. For details on this analytical approach, consult Refs. [10, 15, 16].

2. The NOvA experiment

Chapter 2 provides essential information on the NOvA experiment and its physics interests.

2.1 Introduction and physics interests

NOvA (NuMI Off-axis ν_e Appearance) is a long-baseline accelerator neutrino oscillation experiment using Fermilab's NuMI (Neutrinos at the Main Injector) 700 kW beamline. NOvA has two functionally identical detectors (near and far detector) 14.6 mrad off the beam axis and separated by 810 km of Earth's crust, enough for matter effects to substantially affect $P(\nu_\mu \to \nu_e)$. It observes $\nu_\mu \to \nu_\mu$ and $\nu_\mu \to \nu_e$ transitions in the ν_μ beam, which can run in both ν-beam ($\nu_\mu \to \nu_\mu/\nu_e$) and $\bar{\nu}$-beam ($\bar{\nu}_\mu \to \bar{\nu}_\mu/\bar{\nu}_e$) modes.

The experiment started in 2014, and it is scheduled to run until 2025. NOvA addresses several aspects of neutrino oscillations:

1. the size of $\sin^2 2\theta_{23}$ and $|\Delta m^2_{32}|$,
2. the CP violation, *i.e.*, $\delta_{\text{CP}} \neq 0$,
3. the neutrino mass ordering, *i.e.* the sign of Δm^2_{32}, and
4. the θ_{23} ambiguity, *i.e.*, whether $\theta_{23} =, <$ or $> 45°$.

2.2 The NuMI beam

NuMI is a ν_μ beam operated at Fermi National Laboratory, Illinois, USA, near Chicago (map in Fig. 2.1). Neutrinos are produced in decays of secondary mesons (π and K) from the primary interactions of accelerated, 120 GeV protons from the Main Injector (accelerator) with a graphite target. K and π decay predominantly via

$$\pi^\pm, K^\pm \to \mu^\pm + \nu_\mu/\bar{\nu}_\mu \tag{2.1}$$

and subsequent $\mu^\pm$ decays

$$\mu^\pm \to e^\pm + \nu_e/\bar{\nu}_e + \bar{\nu}_\mu/\nu_\mu. \tag{2.2}$$

The original 350 kW NuMI has been steadily improved since before NOvA started taking data. As of Mar 2020, NuMI works at around 600 kW with the capability of up to 700 kW. That makes it currently the highest intensity artificial neutrino source. A schematic of the NuMI beamline and its main elements is in Fig. 2.2.

2.3 Off-axis concept

Mesons π and K decay isotropically and produce monoenergetic neutrinos in their rest frame. When boosted, neutrino energy E_ν is "less dependent" on the energy of parent π and K as illustrated by Fig. 2.3 – left (detailed derivation in, *e.g.*, Ref. [5]).

Although the integrated off-axis beam flux is reduced, the energy spectrum is much sharper. Depending on the angle, the flux is enhanced at lower and suppressed at higher energies w.r.t. the on-axis geometry, Fig. 2.3 – right. The NOvA detectors sit about 14.6 mrad off the beam axis (at the red curves in Fig. 2.3), which reduces backgrounds with broad energy distribution such as NC events and ν_τ CC events with a threshold over 3 GeV.

The right combination of the beam focusing optics, off-axis angle (14.6 mrad), and sufficient oscillation baseline (810 km) allows NOvA to observe the region of the first oscillation $\nu_\mu \to \nu_\mu$ disappearance minimum and $\nu_\mu \to \nu_e$ appearance maximum in a narrow energy peak around 2 GeV.

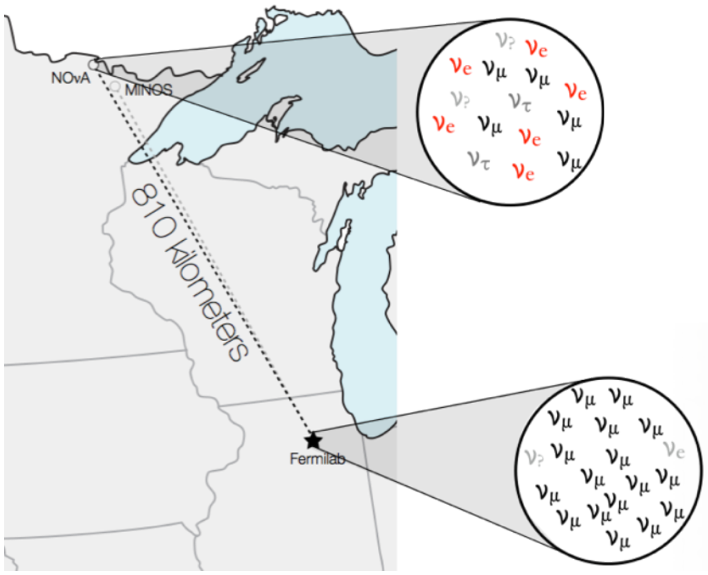

Figure 2.1: Map of NuMI, https://images.app.goo.gl/t8NxrcgyJgbEHrvo8 (as of Feb 2021).

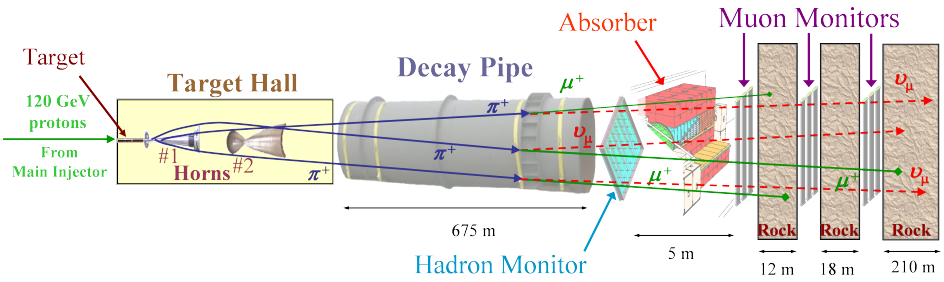

Figure 2.2: Schematic of the NuMI beamline. **From left to right:** 120 GeV protons hit the target, producing π and K. These are focused by magnetic horns, then decay in the Decay Pipe. All hadrons are stopped in the Hadron Absorber, and residual muons are attenuated by rock. The figure was taken from Ref. [17].

2.4 NOvA detectors

NOvA uses two functionally equivalent detectors: Near Detector (ND) and Far Detector (FD). They are both finely segmented, highly active (∼65% active mass), liquid scintillator tracking calorimeters. They are as similar as possible aside from the size, see Fig. 2.4.

The basic detection unit of both detectors is a cell of extruded, highly reflective PVC filled with scintillator and a looped wavelength shifting (WLS) fiber attached to a pixel of an avalanche photodiode (APD), Fig. 2.5. In total, there are ∼344000 cells in the FD and ∼20000 in the ND. The high detector segmentation is vital for a satisfactory tracking resolution of neutrino interaction final states. To compensate for its short length, the ND is equipped with a μ-catcher of several detector planes interlayered with steel at the downstream end of the detector.

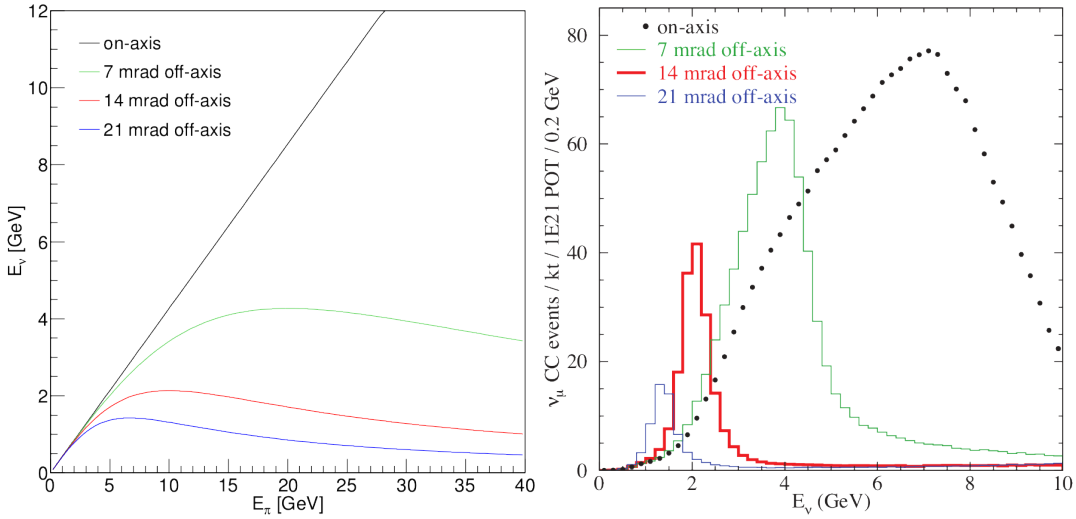

Figure 2.3: NOvA neutrino beam off-axis concept. **Left:** ν_μ energy E_ν as a function of the parent π energy E_π for several experimental off-axis angle dispositions. **Right:** Simulated NuMI neutrino flux for off-axis energy spectra, the figure is from Ref. [18]. NOvA approximately corresponds to the red lines.

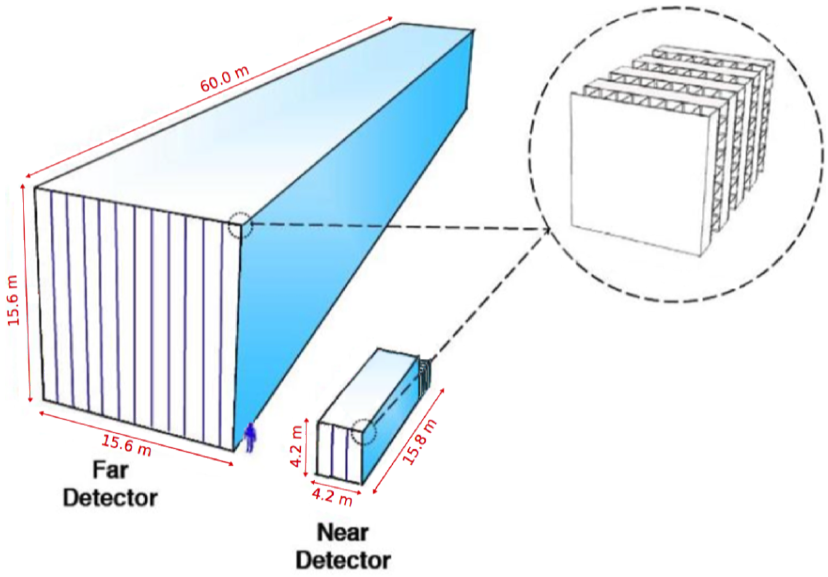

Figure 2.4: Drawing of the NOvA detectors, from Ref. [18].

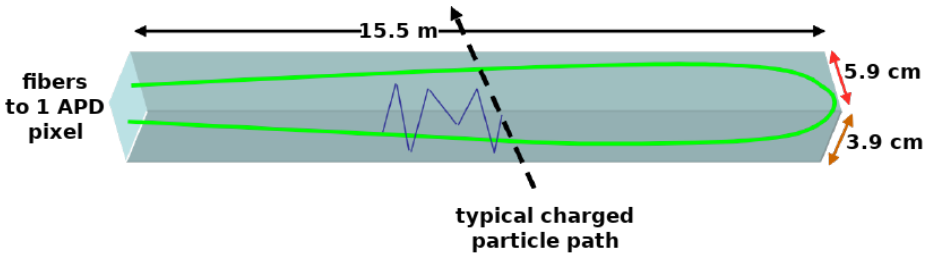

Figure 2.5: Basic NOvA detector unit, detector cell. Extruded reflective PVC filled with scintillator and a looped wavelength shifting fiber, from Ref. [18].

3. The NOvA neutrino oscillation analysis

This chapter outlines the NOvA 2020 neutrino oscillation analysis within the 3ν-paradigm.

3.1 Analysis strategy

The NOvA neutrino oscillation analysis study neutrino transitions over 810 km between its two detectors (near, ND, and far, FD, detector) in four channels: $\nu_\mu \to \nu_\mu$ or $\nu_\mu \to \nu_e$, and $\bar{\nu}_\mu \to \bar{\nu}_\mu$ or $\bar{\nu}_\mu \to \bar{\nu}_e$. With inputs from solar (Δm^2_{21}, θ_{12}) and reactor experiments (θ_{13}), constraints on the oscillation parameters $\Delta m^2_{32}, \theta_{23}$ and δ_{CP} can be deduced from the data.

The ND is used to generate the FD analysis predictions to reduce the detector correlated systematic uncertainties. This course proceeds for two sets of ν-beam and $\bar{\nu}$-beam data and in two separate phases corresponding to two analysis dis/appearance channels.

The following convention is adopted: there are two sets of data with different NuMI horn polarities, **ν-beam** and **$\bar{\nu}$-beam**, two **analysis channels** of ν_μ disappearance and ν_e appearance and several **analysis samples** (fourteen in total) contributing with their **bins** to the final likelihood construction (Section 5.1).

3.2 Improvements and changes in 2020 analysis

The NOvA 2020 analysis involved several updates and upgrades [19] compared to Ref. [20]:

Primary changes:

- New ν-beam data, an increase of approx. 50% in the ν-beam POT (protons-on-target).
- New NuMI high-intensity 900 kW target.
- Upgrade of the neutrino interactions simulation to GENIE v3.0.6 and the NOvA custom model with updated internal tunes.
- Upgrade to a different version of Geant4 v10.4 (+patch 02), light model and readout simulation updates, improvements of the detector calibration procedure.
- New basic clustering algorithm for event reconstruction.
- New additional variable of μ (or e) transverse momentum p_t to the beam direction used to generate FD predictions via Far/Near technique, *i.e.* "extrapolation samples".
- Multiple improvements in systematic uncertainties evaluation and validation.

Secondary changes:

- Retraining and update of all major PID algorithms.
- Reoptimizing the energy estimators.
- Changes and reoptimization of the event selections and decomposition techniques.
- Reevaluation of systematic uncertainties.

3.3 Data sets

The analysis data has accumulated over six years since the start of its taking in 2014. The total ν-beam exposure accounts for 13.60×10^{20} POT of the full FD mass equivalent and 12.50×10^{20} POT for $\bar{\nu}$-beam [21]. There are ten periods of data from 6 Feb 2014 to 14 Mar 2020; two of them are new in the 2020 analysis. With the previous 8.85×10^{20} POT ν-beam exposure [20], the new data represents about one-third of the total ν-beam POT.

3.4 NOvA simulations

To simulate neutrino fluxes and detectors response, NOvA uses a complex simulation chain.

Detailed model of the beamline geometry and Geant4, together as G4NuMI, simulates the hadron production at the beam target and decays into neutrinos. The flux is constrained with data from hadron production experiments by the PPFX (Package to Predict FluX) [22].

Neutrino interactions in the detectors and their vicinity are simulated with GENIE (Generates Events for Neutrino Interaction Experiments) [23, 24]. GENIE was upgraded to v3.0.6[1] and used with an internally constructed "Comprehensive Model Configuration" (CMC) of cross section, hadronization, final state interaction (FSI), and nuclear dynamics models as in Refs. [25, 26]. Cross section model of meson exchange current (MEC) interactions and FSI were tuned to the ND data to improve the overall ND data/MC agreement, Fig. 3.1.

CRY (Cosmic-RaY shower generator) provides cosmic showers and cosmogenic μ [27].

Propagation, energy depositions, and interactions of particles in the detectors are simulated by Geant4 [28, 29, 30], which was upgraded to v10.4 with patch 02.[2] Several custom NOvA procedures model the final signal light collection, attenuation in the fibers, background noise, and response of APDs [31]. A new tuning method was developed and employed in the 2020 analysis for the full NOvA's light collection model [32]. The number of photons produced in the scintillator that is collected by the WLS fiber N_γ is parameterized as

$$N_\gamma = F_{\text{view}}(Y_s E_{\text{Birks}} + \epsilon_C C_\gamma), \tag{3.1}$$

where E_{Birks} is the number of photons produced by scintillation from Birks' empirical law [33], and C_γ are Cherenkov radiation photons calculated from the Frank-Tamm formula [34]. Y_s and ϵ_C are corresponding scaling factors (efficiencies) as the intrinsic properties of the active medium. F_{view} is an overall scaling factor for each of the detector views (top and side) to account for the detector cells' and prevailing μ directions and separately for the ND and FD. All six parameters were deduced from a fit in four dedicated MC and data samples [32].

3.5 Event reconstruction

NOvA's raw data are sets of cell "hits", collected charge with timestamps, Fig. 3.2, mapped to the cells spatial distribution (cells' IDs) in individual exposition windows of triggered time intervals. The hits are taped in two plane projections xz – top view and yz – side view, where z is the direction along the detector length, x is the horizontal, and y the vertical direction perpendicular to z. The frame origin is located in the center of the detector's front face through which the beam enters.

Event reconstruction consists of several consecutive algorithms for clustering, vertexing, and tracking. The reconstruction process also accounts for events filtering to remove dominant backgrounds at the early stages of data processing. Except for the new clustering [36], a sweeping summary of the NOvA reconstruction chain was given in Ref. [37].

[1] For more information on GENIE v3.0.6, visit http://genie-mc.org or the preliminary physics and user manual at https://genie-docdb.pp.rl.ac.uk/DocDB/0000/000002/006/man.pdf (as of Dec 2020).

[2] http://cern.ch/geant4-data/releases/patch_geant4.10.04.p02.tar.gz (as of Jan 2021)

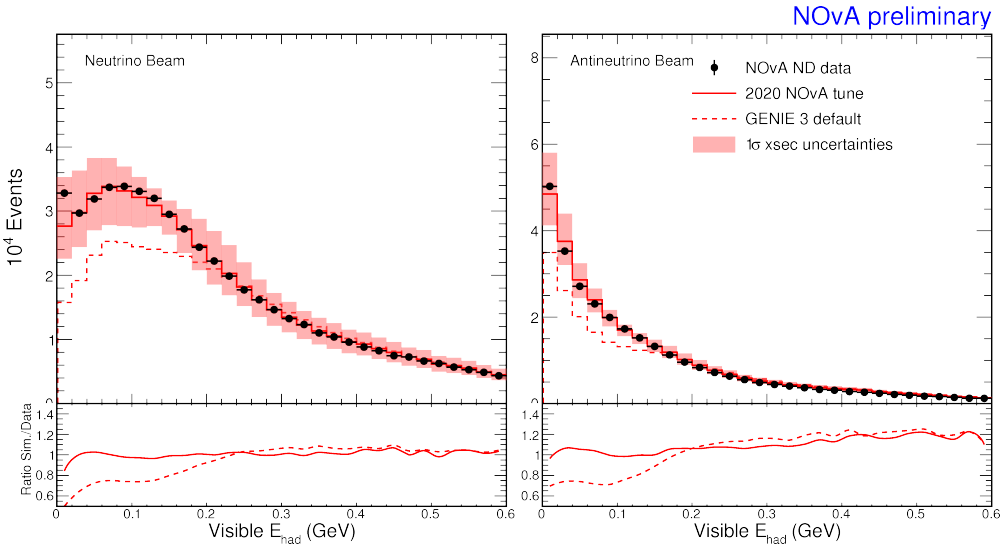

Figure 3.1: Comparisons of default GENIE v3.0.6 simulation (dashed) and internal 2020 NOvA tune (full) in distributions of visible energy of the hadronic system of ND ν_μ CC samples. FSI model and neutrino cross section Valencia MEC model are corrected by ND data (black dots). **Left:** ν-beam. **Right:** $\bar{\nu}$-beam. The plots are from Ref. [35].

Raw hits: Raw hit is any above-threshold charge in ADC units collected by the elementary channels of a detector cell+APD pixel. They also account for the electronic noise.

Hits (CalHits): Raw hits provided with information on geometry, calibration, and optionally on beam and detector conditions become the fundamental data objects.

Slice: Spatially adjacent and in-time close hits are called a slice. Slices serve as the primary candidates of fundamental physics events. There is a new "slicer" (Time Density Slicer) [36] based on a centroid-finding algorithm from Ref. [38]. It is expected to better fight pile-up effects and related reconstruction failures, which might increase the number of ND ν CC candidates by up to 7% compared to previous analyses.

Vertex: Elastic Arms algorithm [40] carries out the vertexing from vertex seeds identified by a modified Multi-Hough transform for recorded hit pairs [39].

Prong: Prong is a collection of hits in a slice to represent a single particle emerging from the interaction vertex. The formation of prongs is arranged by a possibilistic hit clustering with an adjusted Fuzzy K-means algorithm [41].

Tracks: The reconstruction of μ tracks for ν_μ CC interaction candidates uses a simple linear Kalman filter technique [42, 43].

3.6 Detectors energy calibration

The energy calibration of the detectors has two steps [44]. The first one is a cell-by-cell relative calibration which accounts for light attenuation in the long fibers inside the detector cells (attenuation calibration). The second one is the absolute energy calibration (the calorimetric energy scale). They both exploit cosmic data of tri-cell hits in three neighboring and perpendicular detector cells to ensure reasonable estimates of hit positions and energy depositions. To fight the calibration drift (scintillator and electronics aging), the absolute energy scales were newly determined separately for several shorter data-taking intervals.

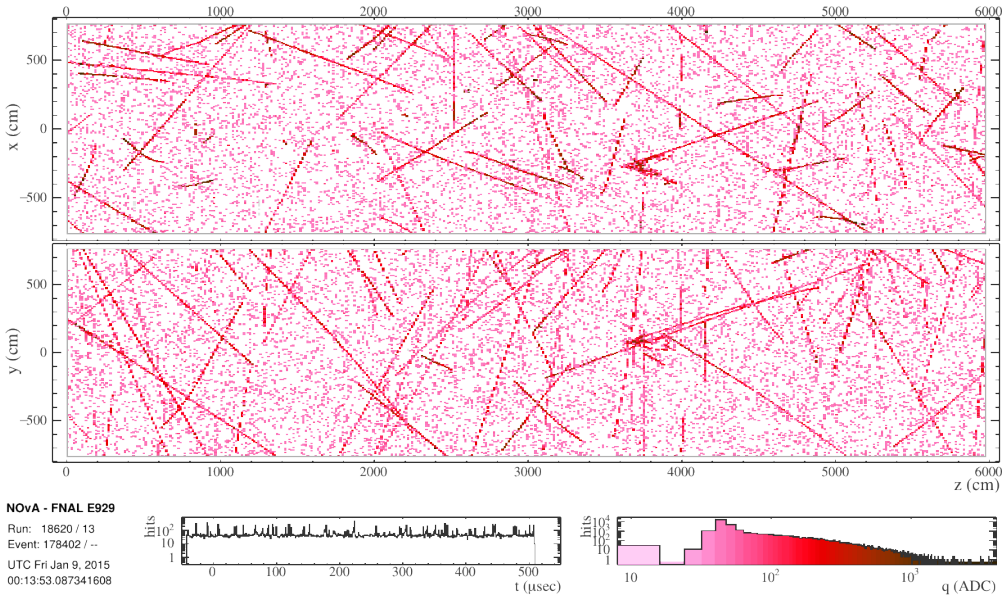

Figure 3.2: Example of the FD data collected in the NuMI trigger 550 μs window in both views xz top (top panel) and yz side (bottom panel). Color brightness corresponds to the collected charge (ADC units). NuMI beam arrives from the left in a spill centered in 218–228 μs. Most of the activity is cosmogenic as the detector is located on the surface.

3.7 Particle identification algorithms

There are two new filters to remove obvious undesirable or background candidates of cosmic [45] and uncontained events [46] from the reconstruction chain. To identify cosmic events within the NuMI trigger window, several cosmic rejection BDTs (Boosted Decision Tree) are employed separately for ν_μ, ν_e and ν-/$\bar{\nu}$-mode data [47, 48]. Furthermore, to distinguish reconstructed Kalman tracks of μ from others (mostly from $\pi^\pm$), NOvA uses the so-called ReMId (Reconstructed Muon Identification) auxiliary BDTG algorithm (Gradient BDT) [49]. ReMId discriminating efficacy is beyond 90% as used in the 2020 analysis.

3.7.1 Convolutional visual networks

To identify and classify neutrino interactions and particles emerging from them, NOvA employs techniques from machine learning and computer vision for image recognition. CVNs (Convolutional Visual Network) are convolutional neural networks (CNN) with visual inputs of calibrated pixel-maps.[3] In the case of NOvA, xz and yz detectors view hit-maps of the reconstructed objects colored pixel-wise by the collected charge serve as inputs to CVNs to construe the typical topological features of the NOvA events. The outputs of the networks are closed sets of classification scores ranging over all eligible hypotheses of the physics events. The scores are normalized to one to provide a "probability-like" interpretation.

There are two CVNs: one for identifying the ν interaction events (event CVN or simply CVN) and one for classification of the reconstructed prongs (prong CVN or pCVN). To train and validate the networks, adequately split between the procedures, about 2.5 million events for each $\nu_\mu + \bar{\nu}_\mu$ CC, $\nu_e + \bar{\nu}_e$ CC and NC, 1.25 million $\nu_\tau + \bar{\nu}_\tau$ CC (not used for event CVN) were generated and ~ 0.75 million cosmic data events were chosen. CVN training technote is in Ref. [50], Refs. [51, 52] document the use of CVN in previous analyses.

The new event CVN has about 90% efficiency and similar purity in terms of the highest

[3] CVN(s) refers to a specific CNN(s) developed by NOvA for neutrino interactions classification.

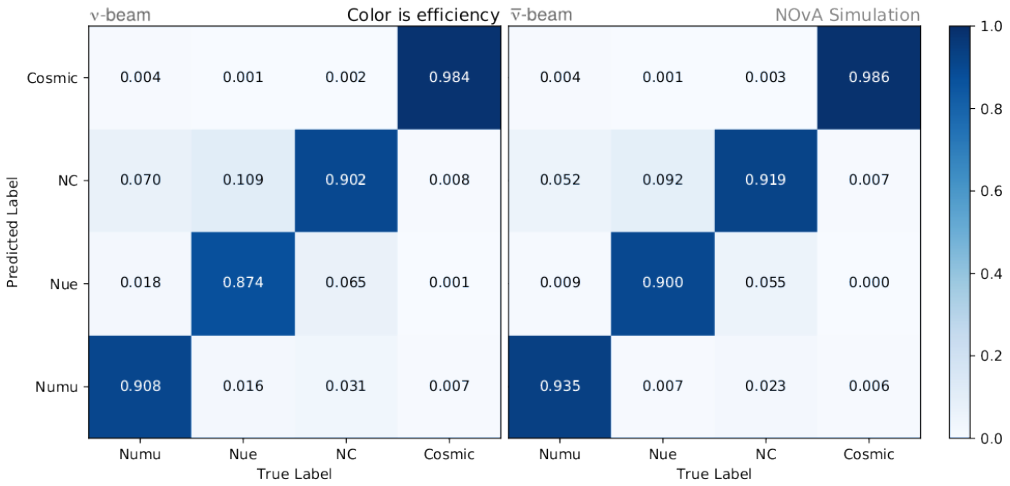

Figure 3.3: Classification efficiency of the event CVN for ν-beam (left) and $\bar{\nu}$-beam (right). The predicted label corresponds to the highest CVN output score (ν_μ CC – Numu, ν_e CC – Nue, NC or cosmic). The plots are from Ref. [53].

classification score of the network's output, Fig. 3.3, pCVN expected efficiency is more than 80% with purity ranging from 78% (γ, π) to over 97% (μ).

3.8 Energy estimation

There are two energy estimators in the oscillation analysis: one for ν_μ and one for ν_e CC candidates. Both were reoptimized because of the modeling and reconstruction changes [54, 55]. The functions were determined for ν- and $\bar{\nu}$-beam modes separately.

The energy of selected ν_μ CC is taken as a sum of the energy of the primary μ E_μ and the remaining activity (hadronic shower) E_{had} [56, 57]

$$E_{\nu_\mu} = E_\mu + E_{\text{had}}. \tag{3.2}$$

E_μ is derived from the reconstructed μ track (Kalman) length. As μ from ν_μ CC interactions are almost ideal MIPs, the average E_μ resolution of about 3% is directly related to the size of the detector cell planes. E_{had} is estimated from all calorimetric energy not assigned to the μ track, *i.e.* visible hadronic energy, and its resolution is about 30%.

The average resolution of the total E_{ν_μ} is approximately 8–11%, depending on the beam mode, detector, and data-taking period [57]. It strongly depends on the $E_{\text{had}}/E_{\nu_\mu}$ fraction, varying from less than 6% (low $E_{\text{had}}/E_{\nu_\mu}$) to more than 12% in the final ν_μ CC samples.

E_{ν_e} is estimated as a quadratic function of the calorimetric contributions of electromagnetic-like prongs E_{em} and hadronic-like prongs E_{had} (discriminated by pCVN)

$$E_{\nu_e} = a_0(a_1 E_{\text{em}} + a_2 E_{\text{had}} + a_3 E_{\text{em}}^2 + a_4 E_{\text{had}}^2). \tag{3.3}$$

The parameters are obtained through a fit to FD MC ν_e CC events. Final ν_e energy resolution is slightly better than in the previous analysis [19], about 10.7% / 8.8% in $\nu/\bar{\nu}$-beam [58].

3.9 Event selection and analysis samples

The analysis utilizes two conceptually different event selection chains for the disappearance (ν_μ selection) and appearance (ν_e selection) channel as illustrated by Fig. 3.4 and in Ref. [59].

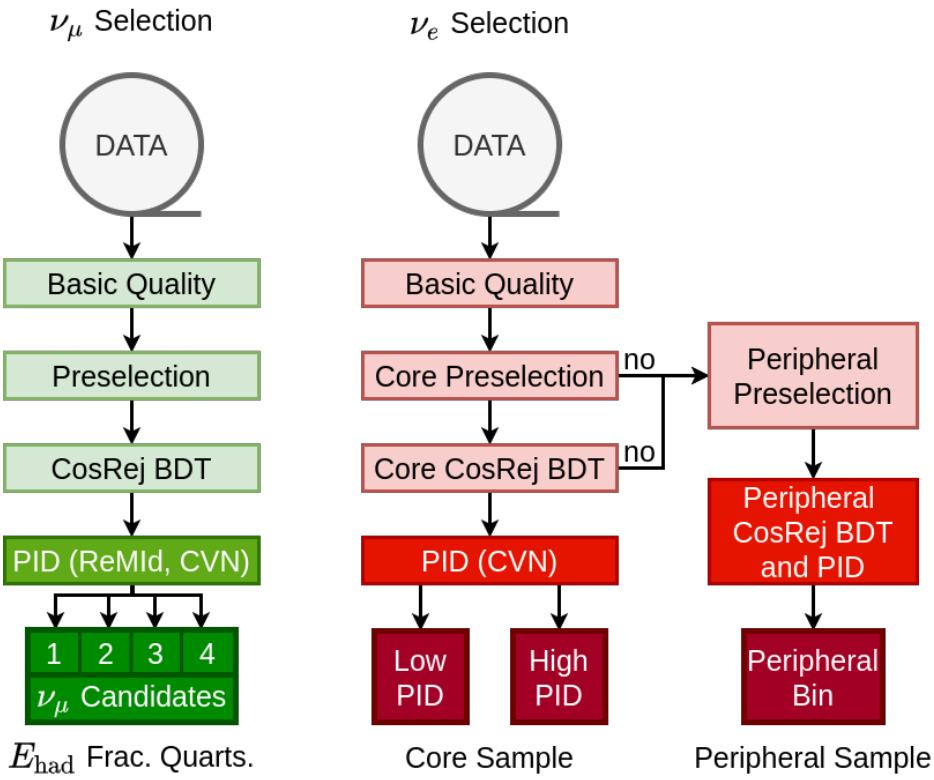

Figure 3.4: Event selection cutflows in the disappearance (left, green, ν_μ selection) and appearance (right, red, ν_e selection) channel. The splitting into the analysis samples of E_{had} fraction quartiles, low/high PID, and the peripheral sample is indicated, see Subsections 3.9, 3.9, and 3.9 for clarification. The selections are similar for ν- and $\bar{\nu}$-beam data.

ν_μ samples

As E_{ν_μ} resolution strongly depends on the $E_{\text{had}}/E_{\nu_\mu}$ fraction, ν_μ CC selections are divided into four subsamples based on the reconstructed $E_{\text{had}}/E_{\nu_\mu}$ called the "hadronic energy fraction quartiles" equally populated in FD MC. It can significantly enhance sensitivity to the important $\sin^2 2\theta_{23}$ [60]. The quartiles are numbered from the lowest $E_{\text{had}}/E_{\nu_\mu}$ (quartile 1) to the highest (quartile 4). Furthermore, ν_μ samples use a variable E_{ν_μ} binning, respecting the oscillation "dip" region in the ν_μ spectra, where the minimum of $P(\nu_\mu \to \nu_\mu)$ from Eq. (1.12) is located. The binning is finer for 1–2 GeV and coarser elsewhere.

Three PID classifiers manage the selection of ν_μ CC candidates: ν_μ cosmic rejection BDT, ReMId and event CVN ν_μ score. All PIDs were reoptimized for the 2020 analysis [59].

ν_e core sample

The ν_e PID selection uses the ν_e cosmic rejection BDT and the event CVN ν_e score. The sample has bins of 0.5 GeV width, and it is divided into two subsets depending on the CVN score: low and high PID. They are expected to have different background compositions with more ν_μ and NC events in the low PID bin. The high PID bin has a better purity of signal events and intrinsic $\nu_e + \bar{\nu}_e$ background. The details are summarized in Ref. [59]. Events filtered by this standard cutflow form the so-called "core sample" of the ν_e CC candidates.

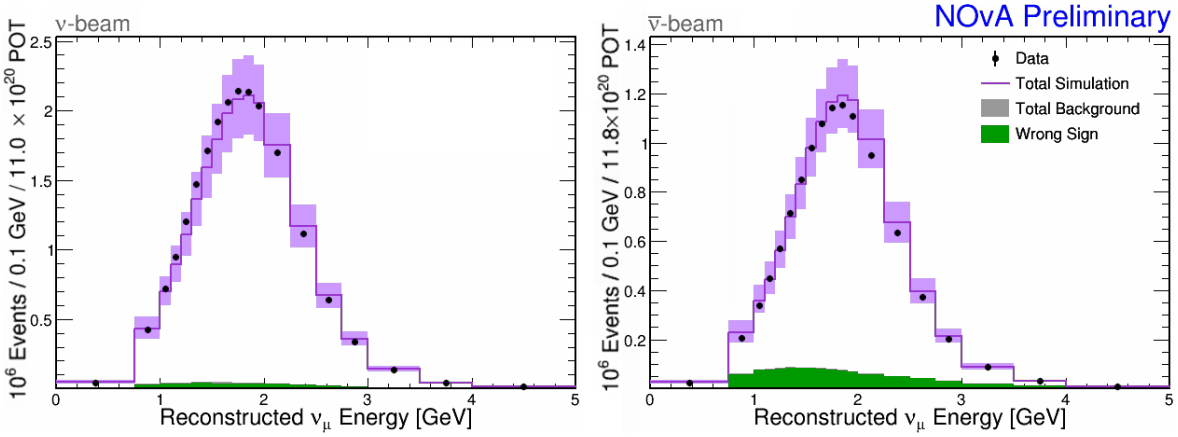

Figure 3.5: Near detector ν_μ CC full selection summed over E_{had} fraction quartiles, *i.e.* number of ND ν_μ CC selected events (black dots) in bins of reconstructed neutrino energy E_{ν_μ} per 0.1 GeV overlaid with MC prediction (violet), wrong sign component of $\bar{\nu}_\mu$ in ν-beam and *vice versa* (green), and the total systematic uncertainty (band). Mostly negligible background (grey) is stacked onto the wrong sign component histogram. **Left:** ν-beam. **Right:** $\bar{\nu}$-beam. The plots are from Ref. [61].

ν_e peripheral sample

Events failing the preselection or ν_e cosmic rejection cuts can still score a very high event CVN ν_e PID. Such events are usually not fully contained, and they appear at the very periphery of the detector. They can be reenacted into the analysis by ν_e "peripheral sample" with looser preselection. As E_{ν_e} cannot be reliably estimated for not fully contained events, they are integrated into a single "counting" peripheral bin. The peripheral sample is expected to contain a significant amount of up to 10% signal events.

3.10 Near detector data constraints and decomposition

ND data is used to directly constrain FD MC predictions in particular analysis samples with the "Far/Near extrapolation" technique. The basic idea of the technique can be simplistically expressed as a correction of FD MC by any ND data/MC discrepancies. FD and ND MC are closely entangled due to the detectors' functional similarity. By imposing equivalent FD event selections in the ND, the analysis FD samples are checked in their unoscillated states to provide information on the neutrino fluxes and interaction rates near the beam source.

To account for the transition probabilities $P(\nu_\alpha \to \nu_\beta)$ en-route to the FD, the constraining ND samples need to be broken down into single components of neutrino flavors (CC) and NC interactions. The procedures are referred to as "decomposition", and they were designed within the individual ND samples. Their intention is to estimate neutrino CC interaction rates of neutrinos with a specific flavor ν_α (or NC interactions) under selection s as a vector in neutrino reconstructed energy bins $\mathbf{N}(\nu_\alpha; s) = (N_1, N_2, \ldots)^\top$ or $\mathbf{N}(\text{NC}; s)$. Here s is usually "equivalent" to one of the FD analysis sample selections.

The complete ND ν_μ CC samples are in Fig. 3.5. They are expected to consist almost entirely of $\nu_\mu + \bar{\nu}_\mu$ CC events. Hence, ν_e CC and NC interactions can be neglected, and the decomposition is a straightforward bin-by-bin proportional data/MC scaling of the $\nu_\mu + \bar{\nu}_\mu$ components to obtain $\mathbf{N}(\nu_\mu; s_\mu)$ (where s_μ is the ND ν_μ selection).

ND ν_e samples represent a ν_e-like contents of the NuMI $\nu/\bar{\nu}$-beam and thereby constrain the beam-induced background of FD ν_e samples. ND ν_e samples are mixtures of beam

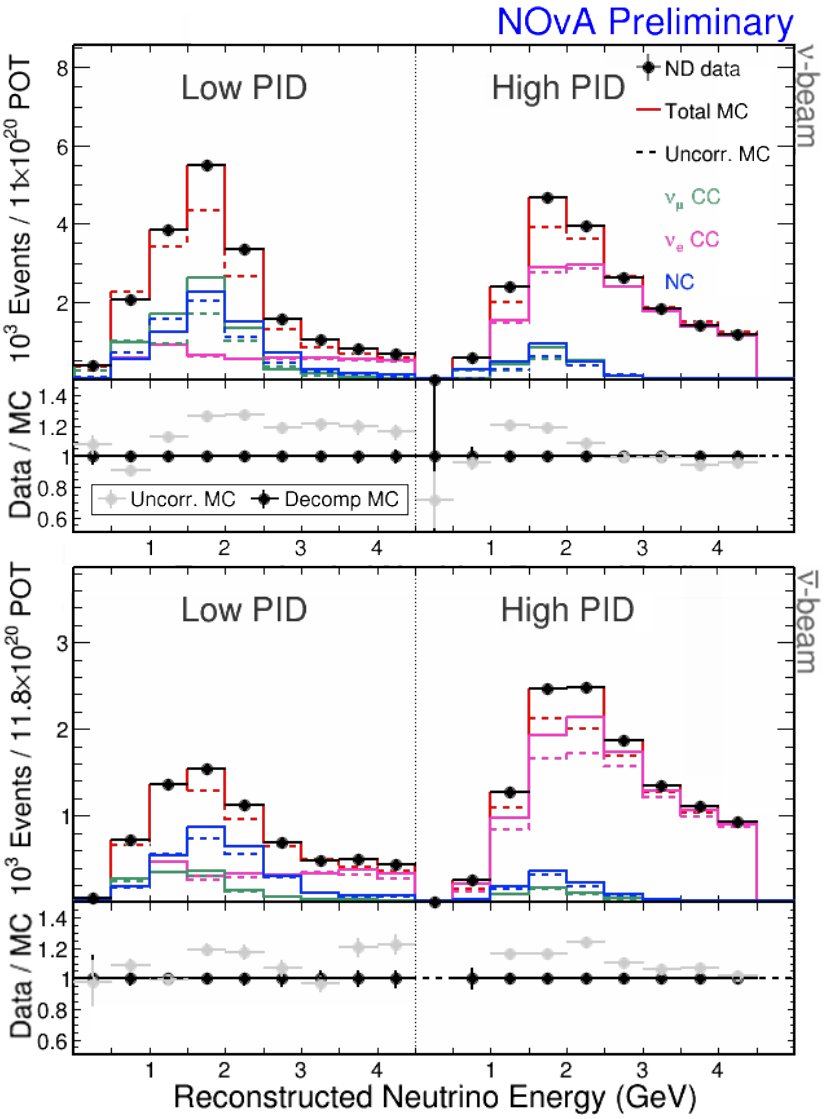

Figure 3.6: ND ν_e CC events of low and high PID score selected samples. The samples are broken down into $\nu_e + \bar{\nu}_e$ (magenta), $\nu_\mu + \bar{\nu}_\mu$ (green) and NC (blue) with the "decomposition" techniques using ND data (black dots) which corrects (full lines) the base MC prediction (dashed lines, grey dots for data/MC). **Left:** ν-beam, BEN+Michel decomposed. **Right:** $\bar{\nu}$-beam, proportionally decomposed. The plots are from Ref. [61].

intrinsic $\nu_e + \bar{\nu}_e$ CC interactions, misidentified $\nu_\mu + \bar{\nu}_\mu$ CC interactions, and NC interactions as seen in Fig. 3.6. Since the expected MC compositions vary significantly by their nature among the samples and in $\nu/\bar{\nu}$-beam, there are three different decomposition methods in use.

Beam ν_e decomposition (BEN): BEN uses dedicated low-energy contained and high-energy uncontained ν_μ CC samples to correct the yields of the parent π and K that decay into both ν_μ and ν_e, *i.e.*, it tracks ν_e and ν_μ common parents to adjust the expected ND ν_e content [62, 63].

Michel decomposition: To fix the ν_μ CC to NC events ratio, the distributions of time-delayed Michel e from μ decays are examined. The $\nu_\mu + \bar{\nu}_\mu$ CC events are expected to contain one extra Michel e on average [63].

Proportional decomposition: Both BEN and Michel decompositions are not directly applicable in $\bar{\nu}$-beam data due to higher contamination of wrong-sign (WS) beam components. Instead, the $\mathbf{N}(\nu_\alpha; s_e)$ are scaled proportionally bin-by-bin with data/MC ratio.

3.11 Near to far extrapolation technique

The technique to generate FD predictions constrained by the ND data is a bit different for predicting signal events (disappearing $\nu_\mu/\bar{\nu}_\mu$, appearing $\nu_e/\bar{\nu}_e$) and beam intrinsic background for ν_e FD samples. They are referred to as "RTR" (reconstructed-true-reconstructed) and "RR" (reconstructed-reconstructed) for the former and latter, respectively.

In the case of RTR, a vector of predicted event rates of ν_β transitioned from ν_α in individual reconstructed energy bins $\mathbf{F_p}(\nu_\alpha \to \nu_\beta; s, f)$ as a single spectrum for a particular selection f and an ND constraining selection s is given by a matrix equation

$$\mathbf{F_p}(\nu_\alpha \to \nu_\beta; s, f) = M_{\mathrm{F}}^{-1}(\nu_\beta/\nu_\alpha; f) \cdot P(\nu_\alpha \to \nu_\beta) \cdot T_{\mathrm{true}}(\nu_\beta/\nu_\alpha; f, s) \cdot M_{\mathrm{N}}(\nu_\alpha; s) \cdot \mathbf{N}(\nu_\alpha; s), \quad (3.4)$$

and the clarification of the individual terms follows; they are illustrated by Fig. 3.7.

$\mathbf{N}(\nu_\alpha; s)$ is the estimated rate of ν_α in ND reconstructed energy bins as a result of the ND decomposition under selection s.

$T_{\mathrm{true}}(\nu_\beta/\nu_\alpha; f, s)$ is a diagonal matrix representing the so-called Far/Near ratio accounting for flux and geometry differences of the detectors w.r.t. the neutrino flavors ν_α, ν_β and ND/FD selections s/f. It is purely simulated with no neutrino transitions applied. And, it is calculated in the bins of true neutrino energies, where ν_α are swapped for ν_β in the simulated flux for FD MC.

$M_{\mathrm{X}}(\nu_\alpha; s)$ are simulated migration matrices from reconstructed to true energy bins for a given neutrino ν_α and a selection s in the ND (M_{N}) and FD (M_{F}).

Finally, $P(\nu_\alpha \to \nu_\beta)$ is a diagonal matrix of $\nu_\alpha \to \nu_\beta$ transition probabilities averaged in the particular true energy bins.

In the case of RR, $\mathbf{F^r_p}$ is calculated similarly, but the Far/Near ratio T_{reco} is applied in the reconstructed neutrino energies

$$\mathbf{F^r_p}(\nu_\alpha \to \nu_\alpha; s, f) = M_{\mathrm{F}}^{-1}(\nu_\alpha; f) \cdot P(\nu_\alpha \to \nu_\alpha) \cdot M_{\mathrm{F}}(\nu_\alpha; f) \cdot T_{\mathrm{reco}}(\nu_\alpha/\nu_\alpha; s, f) \cdot \mathbf{N}(\nu_\alpha; s). \quad (3.5)$$

RR is designed to predict the FD beam intrinsic background of surviving $\nu_e \to \nu_e$, $\nu_\mu \to \nu_\mu$, and NC events misidentified as ν_e CC which are constrained by an equivalent ND selection ($s \approx f$). There is no reason for the ν_e energy estimator to perform well in these samples, so RTR cannot be used.

For the purposes of the F/N technique described above, NC events are considered to be of a non-oscillating neutrino flavor *sui generis*. The beam-induced background of the disappearance ν_μ channel is deduced directly from FD MC as it is expected to be minor if any. So it is in the case of any appearing beam background ($\nu_e \to \nu_\mu/\nu_\tau$, *etc.*) in the ν_e channel. There are also no ν_τ neutrinos assumed in the ND samples.

Extrapolation samples

FD predictions are generated separately for both ν- and $\bar{\nu}$-beams and for all disappearance samples of E_{had} fraction quartiles. The ν_e appearance channel signal and WS background predictions for all low, high PID (core) and peripheral samples use the total ν_μ CC ND selection (summed E_{had}-quartiles) as a constraint. The beam background of the FD ν_e core sample is extrapolated from the corresponding ND ν_e samples. As there is no peripheral ν_e sample in the ND, the high PID ν_e ND sample constrains the FD ν_e peripheral beam background prediction.

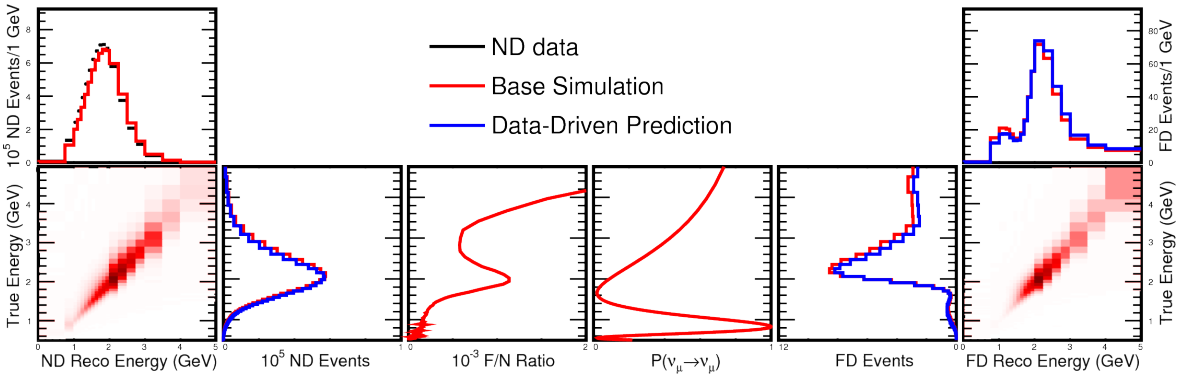

Figure 3.7: Diagram illustrating the Far/Near extrapolation technique for the disappearance channel, Eq. (3.4). **From left to right:** ND sample is decomposed and translated from reconstructed to true neutrino energy (M_{N}), then F/N ratio (T_{true}) and transition probabilities are applied ($P(\nu_\mu \to \nu_\mu)$), and finally, the spectrum is translated back to the reconstructed energy (M_{F}^{-1}). This ND data-driven prediction (blue) works as a correction to the base simulation (red). The diagram is from Ref. [64].

To further increase the analysis robustness and to account for different acceptances and selection efficiencies of the detectors, the signal predictions (and ν_e WS) are extrapolated individually in three p_t subsamples. They are based on the reconstructed transverse momentum $p_t = p\sqrt{1-\cos^2\vartheta}$ of the primary lepton in ν CC interaction candidates, where ϑ is the angle of the lepton direction to the beam direction. The extrapolation p_t samples are then summed back to form the final FD predictions in particular analysis samples [65].

3.12 Unconstrained prediction components and cosmics

Any beam appearing unconstrained background is taken directly from FD MC while weighting by the oscillation probabilities. The cosmic background is estimated from the NuMI sideband timing window around the NuMI beam window containing the accelerator spills. Except for the timing, standard selections are used, and the spectra are scaled to the beam window total livetime. That is done again separately for all analysis samples and ν- and $\bar{\nu}$-beam [66].

3.13 Far detector predictions

The final total FD predictions of the analysis are generated from the ND data constraints if used, and FD MC as *in situ* data objects without specifying the neutrino oscillation parameters. The actual rates in the reconstructed energy bins are estimated by applying the particular neutrino transition probabilities, *i.e.* oscillation parameters, during the validation or the fitting procedure.

With all the analysis changes, the expected gain evaluated in the previous 2019 best fit of oscillation parameters [20] is about +60% both ν-beam ν_μ CC disappearance and ν_e CC appearance events, +20% $\bar{\nu}$-beam $\bar{\nu}_e$ CC events, and a partial loss of −2% $\bar{\nu}$-beam $\bar{\nu}_\mu$ CC.

4. Systematic uncertainties

The following chapter explains the treatment of systematic uncertainties in the NOvA neutrino oscillation analysis, and it reviews and categorizes all of those considered.

4.1 Treatment of systematic uncertainties

There are over one hundred separate systematic "unknowns" studied for the NOvA neutrino oscillation analysis. In the end, about seventy individual uncertainties represented by 67 systematic nuisance parameters were considered. The treatment of systematic uncertainties remained analogous in methodology to the previous oscillation analyses [20] with adequate updates and improvements (new extrapolation samples, better automatization, *etc.*).

In general, both ND and FD MC are modified as positive and negative shifts in terms of the standard deviation ($\pm1\sigma$, $\pm2\sigma$) of the uncertainty relative to the base simulation by

1. reweighting the nominal MC w.r.t. the neutrino interaction type ($\pm1\sigma$, $\pm2\sigma$ shifts, *e.g.* neutrino interaction uncertainties),

2. recalculating the simulated event variables in accordance with the tenet of the particular uncertainty ($\pm1\sigma$, $\pm2\sigma$ shifts, *e.g.* reconstruction uncertainties), or

3. creating a new altered MC events sample by adjusting the simulation parameters (only $\pm1\sigma$ shifts for detector calibration and response uncertainties).

Uncertainties on the final analysis predictions as vectors of neutrino rates in bins of reconstructed energy $\mathbf{F} = (F_1, F_2, \ldots)^\top$ are evaluated by repeating the event selections, decomposition, and F/N technique of Sections 3.9, 3.10, and 3.11, respectively. For each investigated uncertainty, corresponding shifted FD predictions are generated. This approach has a preeminent effect of reducing or even canceling any ND to FD correlated uncertainties thanks to the detectors' functional similarity.

To get the systematically shifted FD predictions at any possible multiples of σ, $\mathbf{F}(\varsigma)$ are parameterized w.r.t. ς of units of a standard deviation σ. The generated shifts are interpolated in $F_i(\varsigma)/F_i(0)$ for all bins of reconstructed energy i and for any tested combination of oscillation parameters with a cubic spline at analysis time [68]. The ς act as the aforementioned systematic nuisance parameter of the subsequent fitting procedure.

The uncertainties were reported as relative changes in integral numbers of predicted events in the analysis samples or channels (*i.e.* summed over subject samples) or as $\pm1\sigma$ shifted spectra in the neutrino reconstructed energy or as a χ^2 test value to the nominal predictions in Ref. [69]. The final evaluations for the best-fit predictions are closely detailed in Ref. [70].

The uncertainties were grouped into categories phenomenologically by their primary sources. Quoted uncertainties are on the total number of predicted neutrino events, approximated or within the ranges for all analysis samples, if not specified.

Detectors calibration: Calibration uncertainties account for the observed energy response data/MC discrepancies in several dedicated control samples (5–7%), different energy responses at the detector cells' ends and in their middle (1–3%), and for the calibration drift, *i.e.* scintillator aging mainly (∼0.5%).

Detectors model: The detector light model suffers from uncertainties on its parameters acquired in additional iterations of the tuning procedure (1–2%) and the uncertainty in the scintillation to Cherenkov light production ratio (<2%).

Neutron uncertainty: An observed ND data/MC discrepancy in a low energy neutron-induced hit clusters in $\bar{\nu}_\mu$ CC candidates enforced an additional uncertainty of about 1% on the $\bar{\nu}_\mu$ CC reconstructed energy (3–5% on FD $\bar{\nu}_\mu$ CC events).

Neutrino cross sections: This category includes all the individual cross section and other neutrino interactions modeling uncertainties, either directly derived from GENIE [24] or developed by the NOvA Cross Section group [25]. Whereas the large ones are considered uncorrelated, the smaller ones are treated with Principal Component Analysis (PCA). PCA uses eigenvalue decomposition of a covariance matrix from an ensemble of randomly generated shifted predictions in neutrino energy bins of Near and Far/Near basis. Identifying the largest principal components helps to account for possible bin-to-bin correlations and reduces the number of systematic nuisance parameters included in the fit (from tens to units), thus reducing computational time. Summed in quadrature, cross section uncertainties are about 2–3% on the total number of predicted events in all the analysis samples.

Beam flux: Uncertainties on the neutrino flux are derived from the beam focusing uncertainties [71] and uncertainties on hadron production at the beam target from the PPFX [22]. They are treated with PCA, altogether accounting for the lowest ones with a <1% effect on the number of predicted events in all analysis samples.

Lepton reconstruction: There are two systematic uncertainties linked to the reconstruction of primary leptons in neutrino CC interactions: μ energy scale from its track length (up to 2.0% for the ν_μ disappearance) [72] and primary lepton angle uncertainty to construct p_t extrapolation samples ($\sim$0.5%, negligible for ν_e appearance).

Near-Far uncorrelated uncertainties: This category lists uncertainties uncorrelated between the detectors and unaffected or introduced by the Far/Near extrapolation technique. Detectors' ν_μ and ν_e acceptance difference probes the plausibility of the ND constraints for the Far/Near extrapolation of ν_e signal ($\sim$0.4–1.0%). Michel tagging uncertainty accounts for mismodeled Michel e candidate reconstruction efficiency (1.5% in ν_e low PID ν-beam sample). Overall normalization suffers from FD active mass, POT counting, and pile-up uncertainties of about 1%. Uncertainties on cosmic and uncontained events prediction components have effects about 1% as well.

4.2 Summary and notes

When summed in quadrature, the expected systematic (statistical) uncertainties on the total numbers of predicted events are 6.5%/6.8% (7%/10%) in the ν_μ disappearance channel and 3.6%/3.8% (10%/17%) in the ν_e appearance channel for $\nu/\bar{\nu}$-beam.

There are several concerns regarding the treatment of the systematic errors in the NOvA neutrino oscillation analysis. Firstly, many uncertainties are estimated on fairly conservative grounds (absolute calibration scale, most importantly). Hence, potential improvements through eventual (and ongoing) studies (NOvA Test Beam) are far from being depleted.

As a matter of fact, the analysis framework does not allow for a straightforward way to deal with possible correlations. The systematic nuisance parameters have to be "decorrelated" (*e.g.* through PCA) upon implementation. That is certainly not true for the whole set in its entirety because of the inadequate effort and time that would be required to do so. Although, this is believed to rather overestimate the final uncertainties, as they are not generally expected to be anticorrelated. Quite the contrary, some uncertainties are suspected of having common sources leading to "double counting", *e.g.* calibration and detector response, normalization, and μ energy scale. The necessary investigations are on the agenda.

Additionally, some uncertainties were designed to "bracket" the related discrepancies and unknowns because their true sources remain unrecognized, *e.g.* calibration shape, neutron uncertainty, or they might be considered not perfectly understood, *e.g.* ND/FD acceptance differences. This could, again, catalyze double counting and ultimate overestimation.

Though the analysis is mainly limited by the experiment's statistics, with about twice the exposure, in the end, further reduction of the systematic uncertainties is still one of the most apparent ways to improve it.

5. Results and constraints on neutrino oscillation parameters

This chapter describes the NOvA neutrino oscillation analysis fitting procedure, the oscillation parameters estimation, and the final results.

The analysis follows a strict blinding policy, and the observations are interpreted within the 3ν-paradigm in terms of the frequentist inference [73].

5.1 Best-fit estimates

The best-fit estimates of oscillation parameters $\boldsymbol{\theta}$ are found by minimizing a log-likelihood ratio $\lambda(\boldsymbol{\theta}, \boldsymbol{\varsigma})$ [3] for n bins of independent Poisson distributed random variables of binned FD data $\mathbf{D} = (D_1, \ldots, D_n)^\top$ and a saturated model $\mathbf{F}(\boldsymbol{\theta}, \boldsymbol{\varsigma})$ of predictions (constructed as in Sections 3.11 to 3.13) with Gaussian penalty terms for systematic parameters $\boldsymbol{\varsigma}$ in units of standard deviation σ

$$-2 \ln \lambda(\boldsymbol{\theta}, \boldsymbol{\varsigma}) = 2 \sum_{i=1}^{n} \left(F_i(\boldsymbol{\theta}, \boldsymbol{\varsigma}) - D_i + D_i \ln \frac{D_i}{F_i(\boldsymbol{\theta}, \boldsymbol{\varsigma})} \right) + \sum_{j=1}^{m} \varsigma_j^2, \tag{5.1}$$

where i runs over the reconstructed energy bin indices ($n = 178$ in total) of all the analysis samples, *i.e.* all analysis bins, and j runs over the systematic nuisance parameters and external constraints ($m = 67 + 1$).

The analysis is performed within the 3ν-paradigm described in Section 1.2. Eq. (5.1) is minimized w.r.t. three neutrino oscillation parameters $\theta_{23}, \Delta m^2_{32}, \delta_{\mathrm{CP}}$, all systematic nuisance parameters $\boldsymbol{\varsigma}$, and one additional parameter with a Gaussian penalty term similar to ς_j for an external constraint on mixing angle θ_{13} from reactor neutrino experiments as in Ref. [74]. All remaining oscillation [74] and experimental parameters are taken as fixed, $L = 810$ km, $\rho = 2.84$ g/cm^3.

Using NOvA FD data, the found **best-fit estimates** are

$$\begin{aligned} \Delta m^2_{32} &= 2.41 \times 10^{-3} \text{ eV}^2, \\ \sin^2 \theta_{23} &= 0.57, \\ \delta_{\mathrm{CP}} &= 0.82\pi. \end{aligned} \tag{5.2}$$

5.2 Far detector data

There were 211 candidates selected in FD ν-beam data for the ν_μ disappearance channel, 105 candidates in $\bar{\nu}$-beam data. There were 82 candidates in ν-beam data for the ν_e appearance channel, 33 for $\bar{\nu}$-beam. The expected total signal+background is 213.7+8.6 for ν_μ disapp. ν-beam, 103.2+2.2 for $\bar{\nu}_\mu$ disapp. $\bar{\nu}$-beam, 59.0+26.8 for ν_e app. ν-beam and 19.2+14.0 for $\bar{\nu}_e$ app. $\bar{\nu}$-beam. That represents over 4σ direct evidence of $\bar{\nu}_\mu \to \bar{\nu}_e$ transition, best among recent neutrino oscillation experiments.

Reconstructed neutrino energy spectra in all analysis samples ($\nu/\bar{\nu}$-beam ν_μ disappearance E_{had}-quartiles and ν_e appearance PID samples) overlayed with the best-fit FD predictions including systematic uncertainty bands are in Figs. 5.1 and 5.2. They are also summarized in Tables 5.1 and 5.2.

Systematic uncertainties were evaluated using the best-fit neutrino oscillation parameters estimates, including the systematic pulls. To this end, $\pm 1\sigma$ limits relative to the best-fit predictions were calculated, eventually summed in quadrature in their categories. Apart from the

Table 5.1: Integral numbers of FD data (bold) and predicted events in the ν_μ disappearance channel analysis samples, Q1–4 E_{had} fraction quartiles, evaluated at the NOvA 2020 best-fit point of neutrino oscillation parameters $\Delta m^2_{32} = 2.41 \times 10^{-3}$ eV^2, $\sin^2\theta_{23} = 0.57, \delta_{\text{CP}}/\pi = 0.82$ (+systematic parameters) and stated exposures for ν- and $\bar{\nu}$-beam.

Disappearance channel FD data and predictions at 2020 best fit								
	Components		Q1	Q2	Q3	Q4	Total	POT-eq.
ν-beam	Signal	$\nu_\mu \to \nu_\mu$	45.92	45.66	49.60	59.87	201.05	13.60×10^{20}
		$\bar{\nu}_\mu \to \bar{\nu}_\mu$	5.79	2.76	2.55	1.53	12.63	
	Bkg.	NC	0.11	0.17	0.42	1.87	2.57	
		Cosmic	0.35	0.35	0.86	3.40	4.96	
		Other	0.21	0.24	0.25	0.40	1.10	
	Total		52.38	49.18	53.68	67.07	222.31	
	Data		**48**	**48**	**40**	**75**	**211**	
$\bar{\nu}$-beam	Signal	$\bar{\nu}_\mu \to \bar{\nu}_\mu$	23.06	19.03	17.78	17.31	77.18	12.50×10^{20}
		$\nu_\mu \to \nu_\mu$	4.03	4.99	6.11	10.92	26.05	
	Bkg.	NC	0.02	0.04	0.10	0.65	0.81	
		Cosmic	0.06	0.03	0.11	0.74	0.94	
		Other	0.08	0.10	0.11	0.15	0.44	
	Total		27.25	24.19	24.21	29.77	105.42	
	Data		**26**	**23**	**27**	**29**	**105**	

1σ systematic bands to be seen in the reconstructed energy plots, overall uncertainties on the integrated predictions in the analysis samples and the expected impact on the uncertainties of the oscillation parameters estimates are shown in Figs. 5.3 and 5.4.

One can directly make several important first-order conclusions. Notably, ν_μ disappearance channel systematic uncertainties are already comparable to the statistical ones, with only about 41% of the total expected NOvA exposure (until 2025). The ν_e appearance channel uncertainties are governed by the low statistics, mainly due to the reduction of neutrino fluxes and cross sections errors through the F/N extrapolation technique. On the other hand, ν_μ disappearance uncertainties are primarily trimmed by flux and cross section PCAs, which employ F/N ratios as well. The subsequent F/N extrapolation effects are lower.

It is evident from Fig. 5.4 that the most significant systematic uncertainty on the neutrino parameters estimates comes from the detector calibration category. Its reduction by better calibration procedure or detector model and alike is vital for more precise $\sin^2\theta_{23}$ measurement or $\sin^2\theta_{23}$ ($\lesseqgtr 0.5$) octant determination. To correctly interpret the comparisons to the reported statistical uncertainties, one should keep in mind the potential "degenerate-like" solutions of the NOvA $\nu_e/\bar{\nu}_e$ appearance problem with different combinations of the θ_{23} octant, δ_{CP} and neutrino masses ordering (hierarchy) hypotheses. In this sense, *e.g.*, the large statistical uncertainties in δ_{CP} are caused by multiple local minima of the Eq. 5.1 function in the parametric space very close to each other in terms of δ_{CP} value.

5.3 Constraints on neutrino oscillation parameters

As the requirements of Wilks' theorem might be unmet because of the low statistics, physical boundaries of the parametric space of interest, *etc.*, and its application is questionable, the confidence level (CL) limits on the estimated parameters are determined by Feldman-Cousins

Table 5.2: Integral numbers of FD data (bold) and predicted events in the ν_e appearance channel analysis samples evaluated at the NOvA 2020 best-fit point of neutrino oscillation parameters $\Delta m^2_{32} = 2.41 \times 10^{-3}$ eV^2, $\sin^2\theta_{23} = 0.57, \delta_{\rm CP}/\pi = 0.82$ (+systematic parameters) and stated exposures for ν- and $\bar{\nu}$-beam.

Appearance channel FD data and predictions at 2020 best fit							
	Components		Low PID	High PID	Peripheral	Total	POT-eq.
ν-beam	Signal	$\nu_\mu \to \nu_e$	10.21	40.49	8.27	58.97	13.60×10^{20}
	WS bkg.	$\bar{\nu}_\mu \to \bar{\nu}_e$	0.19	0.66	0.19	1.04	
	Beam bkg.	$\nu_e + \bar{\nu}_e$	2.49	7.85	3.74	14.08	
		$\nu_\mu + \bar{\nu}_\mu$	1.12	0.31	0.28	1.72	
		$\nu_\tau + \bar{\nu}_\tau$	0.16	0.26	0.10	0.52	
		NC	4.42	1.52	0.37	6.31	
	Cosmic		1.28	0.21	1.64	3.13	
	Total		19.88	51.29	14.60	85.77	
	Data		**16**	**50**	**16**	**82**	
$\bar{\nu}$-beam	Signal	$\bar{\nu}_\mu \to \bar{\nu}_e$	2.21	14.13	2.83	19.18	12.50×10^{20}
	WS bkg.	$\nu_\mu \to \nu_e$	0.42	1.43	0.40	2.25	
	Beam bkg.	$\nu_e + \bar{\nu}_e$	1.14	4.16	1.98	7.29	
		$\nu_\mu + \bar{\nu}_\mu$	0.17	0.06	0.12	0.35	
		$\nu_\tau + \bar{\nu}_\tau$	0.08	0.17	0.07	0.32	
		NC	1.64	0.44	0.13	2.21	
	Cosmic		0.43	0.14	0.98	1.55	
	Total		6.10	20.53	6.51	33.14	
	Data		**13**	**18**	**2**	**33**	

"Unified Approach" (FC corrections) as in Ref. [77]. The resulting constraints on the neutrino oscillation parameters are found by profiling over any nuisance parameters, including systematics. The constraints are presented, *e.g.*, as contours of 2D allowed regions for two parameters of interest at different CL, usually in terms of 1σ, 2σ, 3σ as 68.27%, 95.45%, 99.73% CL, respectively.

Fig. 5.5 shows the 90% CL region in Δm^2_{32} *vs.* $\sin^2\theta_{23}$ with comparisons to the latest results of T2K [13], MINOS+ [78], IceCube [79], and Super-Kamiokande [80] neutrino oscillation experiments. They are all in excellent agreement. Fig. 5.6 indicates the 1σ, 2σ, and 3σ allowed regions in $\sin^2\theta_{23}$ *vs.* $\delta_{\rm CP}$ plane for the normal and inverted neutrino mass orderings.

To summarize, there is a large region of the parametric space around $\delta_{\rm CP} \sim \pi/2$ rejected at $>3\sigma$ for IO (IH), Fig. 5.6. Nevertheless, the overall constraints on $\delta_{\rm CP}$ are relatively weak, with any possible value of $[0, 2\pi]$ interval allowed within 2σ. Δm^2_{32} and $\sin^2\theta_{23}$ 1σ allowed regions are estimated as

$$\begin{aligned} \sin^2\theta_{23} &= 0.57^{+0.05}_{-0.07}, \\ \Delta m^2_{32} &= (2.41 \pm 0.07) \times 10^{-3}\ \text{eV}^2. \end{aligned} \tag{5.3}$$

As the best fit corresponds to the NO (NH) and $\theta_{23} > 45^\circ$, rejection significances of IO (IH) and $\theta_{23} < 45^\circ$ were calculated to be both disfavored at about 1σ. The results are consistent with the 2019 analysis in Ref. [20] within 1σ.

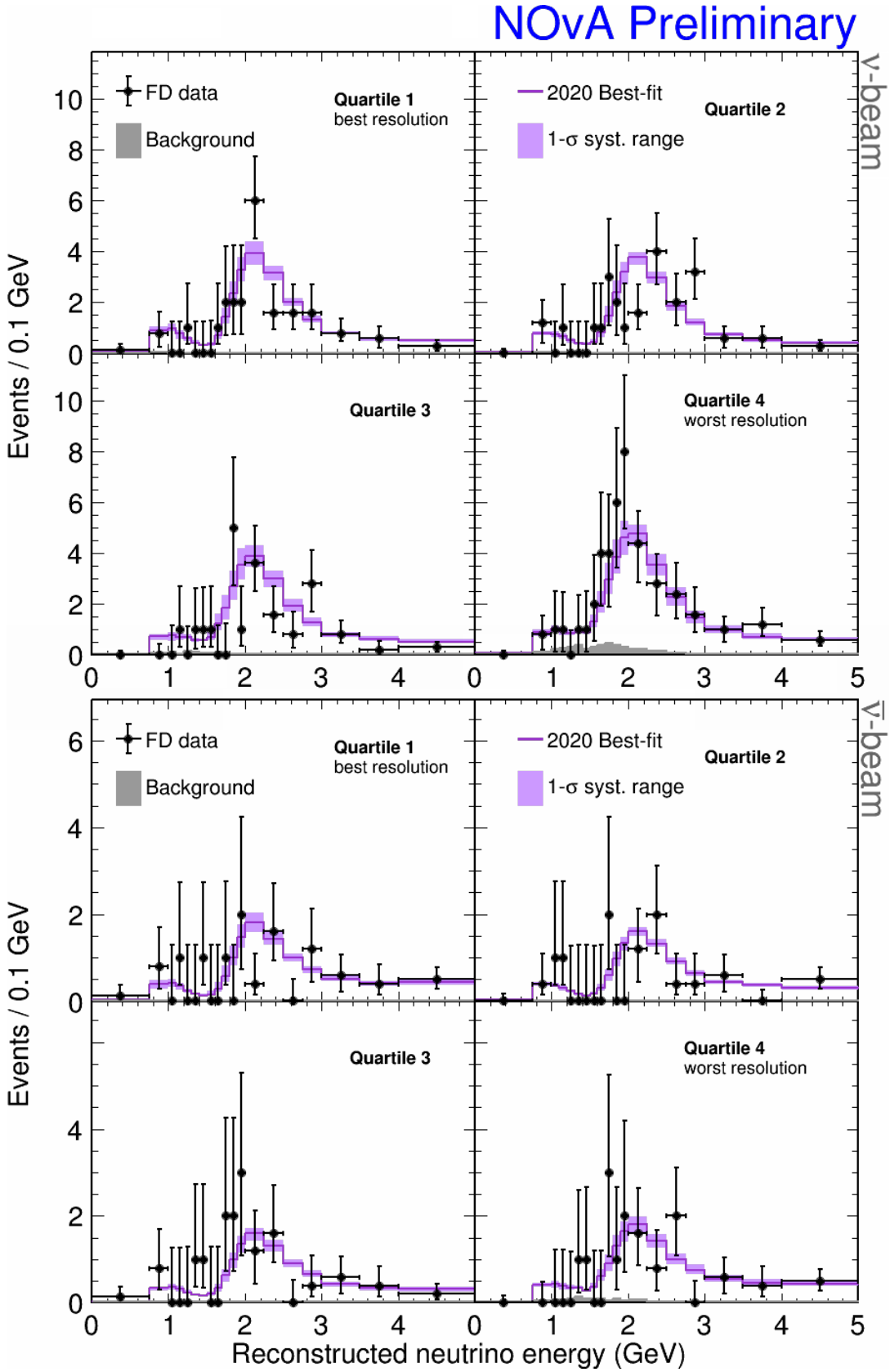

Figure 5.1: Reconstructed energy spectra of the FD ν_μ disappearance channel data selected candidates (black) in individual analysis samples (E_{had} fraction quartiles) overlayed with the best-fit prediction (magenta). **Top:** ν-beam data, four quartiles. **Bottom:** $\bar{\nu}$-beam data, four quartiles. 1σ systematic bands are constructed from the individual uncertainties 1σ limits around the prediction summed in quadrature. Statistical uncertainties are Poisson and FC corrected for the bins with low statistics. The plots are from Ref. [75].

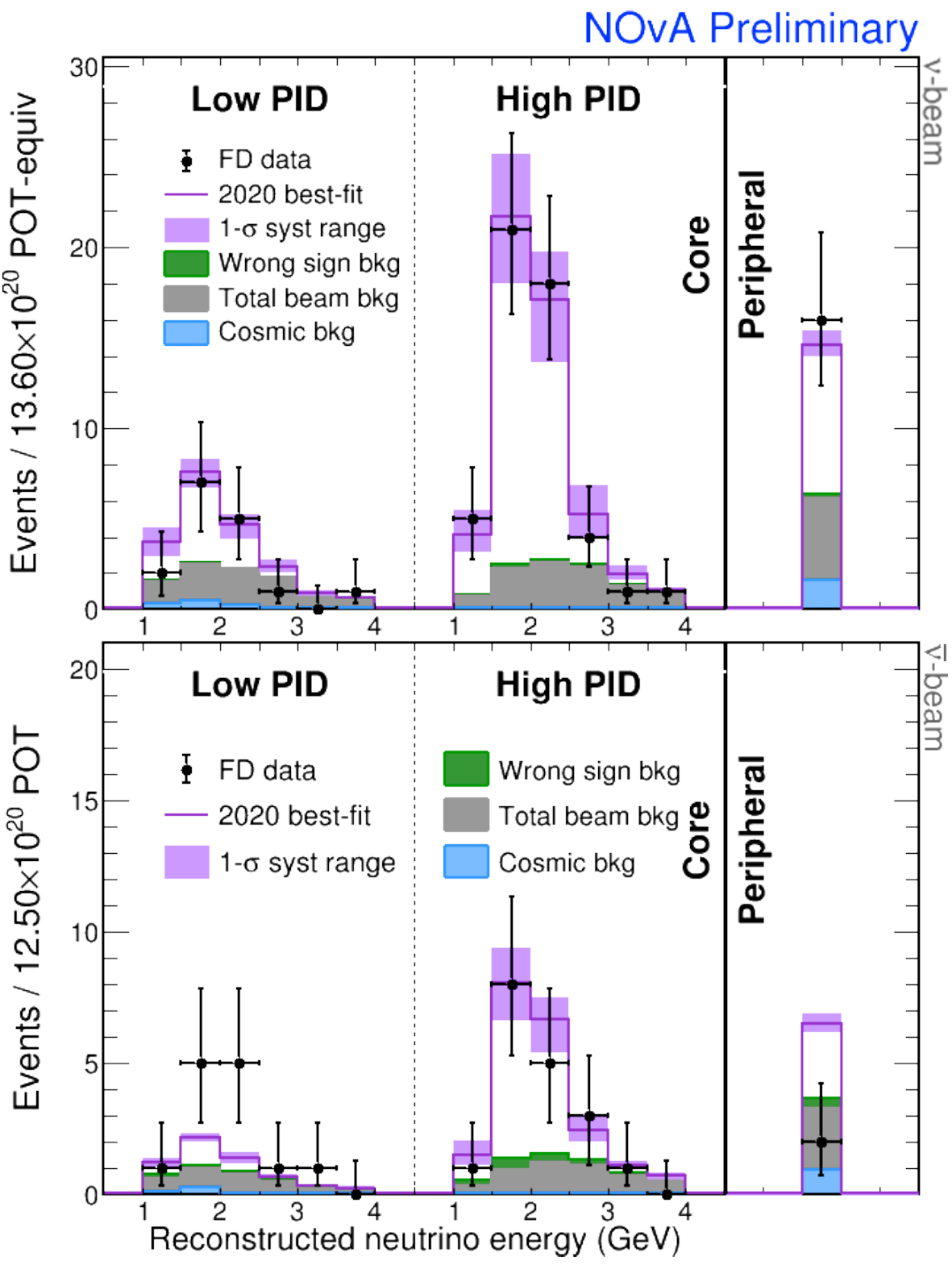

Figure 5.2: Reconstructed energy spectra of the FD ν_e appearance channel data selected candidates (black) overlayed with the best-fit prediction (magenta). The spectra are split into individual low, high ν_e CC PID and peripheral analysis samples. **Top:** ν-beam data. **Bottom:** $\bar{\nu}$-beam data. 1σ systematic bands are constructed from the individual uncertainties 1σ limits around the prediction summed in quadrature. Statistical uncertainties are Poisson and FC corrected for the bins with low statistics. The plots are from [76]

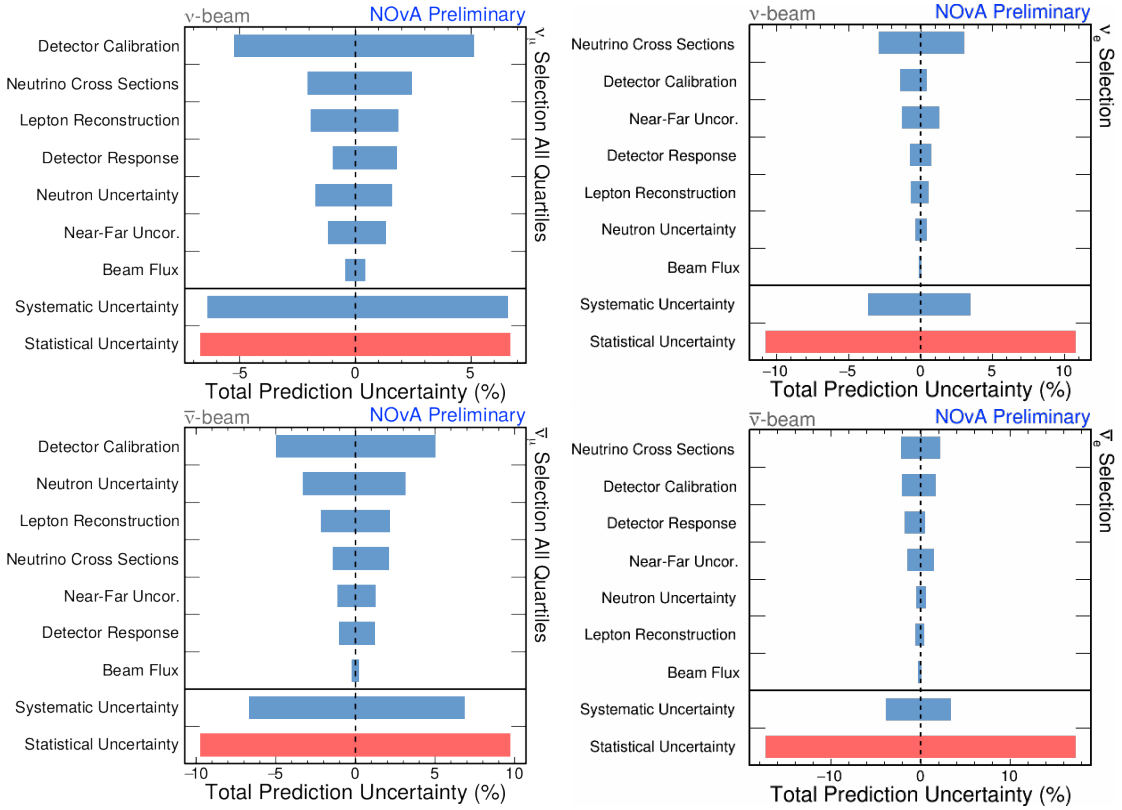

Figure 5.3: Comparisons of the relative systematic (blue) and statistical (red) uncertainties on the total number of predicted events in the ν_μ (left) and ν_e channel (right), ν-beam (top), and $\bar{\nu}$-beam (bottom), evaluated in the NOvA 2020 best-fit point.

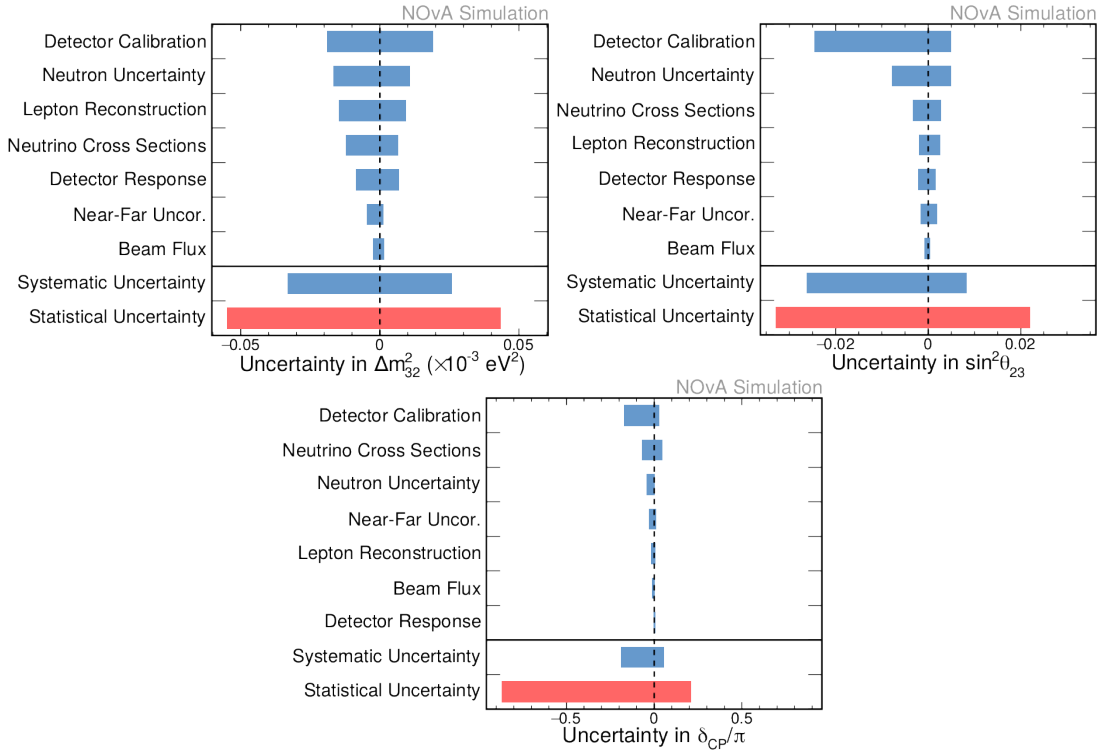

Figure 5.4: Estimated 1σ uncertainties on the neutrino oscillation parameters simulated around the NOvA 2020 best-fit point. **Clockwise from top left:** Δm^2_{32}, $\sin^2\theta_{23}$ and δ_{CP}.

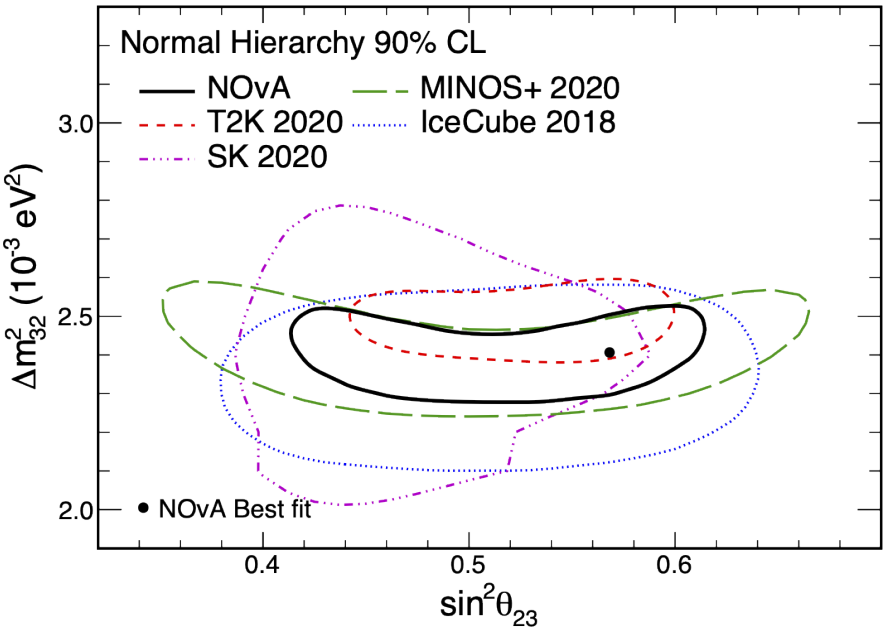

Figure 5.5: NOvA 2020 90% CL contour for Δm^2_{32} *vs.* $\sin^2\theta_{23}$ in the $\Delta m^2_{32} > 0$ hyperplane (black, full) and the best-fit point of $\Delta m^2_{32} = 2.41 \times 10^{-3}$ eV^2, $\sin^2\theta_{23} = 0.57$ (black dot), compared to the latest results from T2K (red, short-dashed), MINOS+ (green, long-dashed), IceCube (blue, dotted), and Super-Kamiokande (magenta, dash-dotted, SK), references in the text. The plot is from Ref. [81].

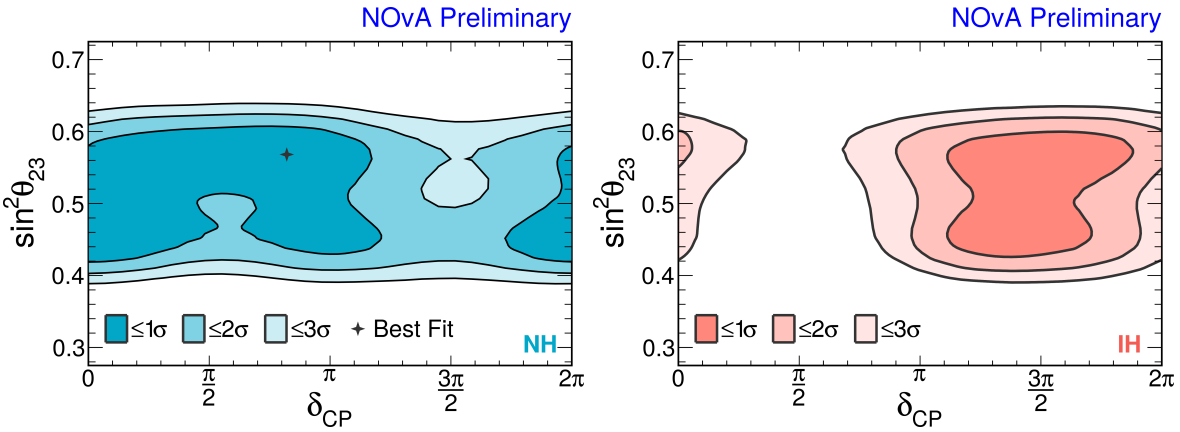

Figure 5.6: NOvA 2020 1σ, 2σ, and 3σ (68.27%, 95.45%, 99.73%) CL contours for $\sin^2\theta_{23}$ *vs.* δ_{CP} for the normal (NH, blue, left) and inverted (IH, red, right) ordering (hierarchy) of the neutrino masses (Δm^2_{32} >0 and <0 hyperplanes). They are profiled over $|\Delta m^2_{32}|$ and the external reactor neutrino oscillation constraint $\sin^2 2\theta_{13} = 0.085 \pm 0.003$ [74] and systematics. The best fit corresponds to $\sin^2\theta_{23} = 0.57$ and $\delta_{CP} = 0.82\pi$. A large portion of the parametric space around $\delta_{CP} \sim \pi/2$ for IH is rejected at $>3\sigma$. The plots are from Ref. [82].

Conclusion

The NOvA experiment presented new results of the neutrino oscillation analysis within the model of three active neutrinos in 2020. This update used new data with about 50% more ν-beam mode of NuMI POT (protons-on-target) and its high-intensity upgrade to 700 kW power. In total, the data represents 13.60 $\times 10^{20}$ POT of ν-beam and 12.50 $\times 10^{20}$ POT of $\bar{\nu}$-beam, accounting for about 41% of the total exposure expected until 2025. The text overviewed the important analysis novelties and the work done for estimating and validating the systematic uncertainties. Although statistical uncertainties currently dominate, understanding the major sources of systematic uncertainties, their correlations, and proper evaluation are vital for both the interpretation and precision of the results and further improvements of the analysis.

There were 211 candidate events observed in the ν-beam ν_μ disappearance, 105 in the $\bar{\nu}$-beam $\bar{\nu}_\mu$, 82 in the ν-beam ν_e appearance, and 33 in the $\bar{\nu}$-beam $\bar{\nu}_e$ appearance channel. Exploiting the NOvA two detector design with the Near to Far Detector extrapolation technique (F/N technique) to generate the analysis predictions, three neutrino oscillation parameters were estimated and constrained. With external inputs on the neutrino squared mass-splitting Δm^2_{21} and mixing angle θ_{12} from the solar experiments, and on the mixing angle θ_{13} from the reactor experiments, the best fit corresponds to

$$\begin{aligned} \sin^2\theta_{23} &= 0.57^{+0.05}_{-0.07}, \\ \Delta m^2_{32} &= (2.41 \pm 0.07) \times 10^{-3}\ \text{eV}^2, \\ \delta_{\text{CP}} &= 0.82\pi, \end{aligned} \tag{5.4}$$

and the normal ordering of the neutrino masses. The parameter δ_{CP} is only poorly constrained with all possible values $[0, 2\pi]$ allowed within 2σ CL. The rest are in good agreement with other neutrino oscillation measurements. The results reject the hypothesis of the inverted mass ordering of the neutrino masses and δ_{CP} around $\pi/2$ at $>3\sigma$ CL. Overall, both lower octant of $\theta_{23} < 45^\circ$ and inverted ordering are disfavored at about 1σ CL. The significances and constraints in the neutrino oscillation parametric space of $\sin^2\theta_{23}$ *vs.* Δm^2_{32}, $\sin^2\theta_{23}$ *vs.* δ_{CP} were detailed in Figs. 5.5, 5.6, respectively.

References

[1] C. Burgess and G. Moore, *The Standard Model: A Primer*, Cambridge books online, Cambridge University Press (2007), ISBN 9780521860369

[2] S. Bilenky, *Introduction to the Physics of Massive and Mixed Neutrinos*, Lecture Notes in Physics, 2nd ed., Springer International Publishing (2018), ISBN 9783319748016

[3] P. Zyla *et al.* [Particle Data Group], Prog. Theor. Exp. Phys. **2020**, 083C01 (2020), 10.1093/ptep/ptaa104

[4] C. Giunti and C. W. Kim, *Fundamentals of Neutrino Physics and Astrophysics*, Oxford University Press (2007)

[5] K. Zuber, *Neutrino Physics*, 3rd ed., CRC Press (2020), ISBN 9781315195612, 10.1201/9781315195612

[6] J. W. F. Valle and J. Romao, *Neutrinos in High Energy and Astroparticle Physics*, Physics textbook, Wiley (2015), ISBN 9783527411979

[7] M. C. Gonzalez-Garcia, AIP Conf. Proc. **917**, 3 (2007), 10.1063/1.2751934

[8] C. Giunti and M. Laveder, 2003, arXiv:hep-ph/0310238

[9] L. Wolfenstein, AIP Conf. Proc. **52**, 108 (1979), 10.1063/1.31797

[10] M. Blennow and A. Y. Smirnov, Adv. High Energy Phys. **2013**, 972485 (2013), arXiv:1306.2903 [hep-ph]

[11] E. K. Akhmedov, JHEP **02**, 107 (2021), arXiv:2010.07847 [hep-ph]

[12] I. Esteban, M. C. Gonzalez-Garcia, M. Maltoni, T. Schwetz, and A. Zhou, JHEP **09**, 178 (2020), arXiv:2007.14792 [hep-ph]

[13] P. Dunne, Latest Neutrino Oscillation Results from T2K, 2020, 10.5281/zenodo.4154355

[14] K. Abe *et al.* [T2K], Nature **580**, 339 (2020), arXiv:1910.03887 [hep-ex], [Erratum: Nature **583**, E16 (2020)]

[15] M. Freund, Phys. Rev. D **64**, 053003 (2001), arXiv:hep-ph/0103300

[16] E. K. Akhmedov, R. Johansson, M. Lindner, T. Ohlsson, and T. Schwetz, JHEP **2004**, 078–078 (2004), 10.1088/1126-6708/2004/04/078

[17] R. M. Zwaska, *Accelerator Systems and Instrumentation for the NuMI Neutrino Beam*, PhD thesis, Texas U., 2005, 10.2172/879065

[18] D. S. Ayres *et al.*, 2007, 10.2172/935497

[19] M. Baird, L. Suter, and J. Wolcott, 2020, NOVA-doc-44422-v3

[20] M. A. Acero *et al.* [NOvA], Phys. Rev. Lett. **123**, 151803 (2019), arXiv:1906.04907 [hep-ex]

[21] A. Back, R. S. Bowles, M. Elkins, B. Ramson, and S. Sanchez, 2020, NOVA-doc-44226-v1

[22] L. Aliaga *et al.* [MINERvA], Phys. Rev. D **94**, 092005 (2016), 10.1103/PhysRevD.94.092005

[23] C. Andreopoulos *et al.* [GENIE], Nucl. Instrum. Meth. A **614**, 87 (2010), arXiv:0905.2517 [hep-ph]

[24] C. Andreopoulos *et al.* [GENIE], 2015, arXiv:1510.05494 [hep-ph]

[25] K. Bays *et al.*, 2020, NOVA-doc-43962-v3

[26] M. Dolce, H. Gallagher, and J. Wolcott, 2020, NOVA-doc-43724-v4

[27] C. Hagmann, D. Lange, and D. Wright, Cosmic-ray shower generator (CRY) for Monte Carlo transport codes, in *2007 IEEE Nuclear Science Symposium Conference Record*, Vol. 2, pp. 1143–1146, 2007, 10.1109/NSSMIC.2007.4437209

[28] S. Agostinelli *et al.* [Geant4], Nucl. Instrum. Meth. A **506**, 250 (2003), 10.1016/S0168-9002(03)01368-8

[29] J. Allison *et al.* [Geant4], IEEE Trans. Nucl. Sci. **53**, 270 (2006), 10.1109/TNS.2006.869826

[30] J. Allison *et al.* [Geant4], Nucl. Instrum. Meth. A **835**, 186 (2016), 10.1016/j.nima.2016.06.125

[31] A. Aurisano *et al.* [NOvA], J. Phys. Conf. Ser. **664**, 072002 (2015), 10.1088/1742-6596/664/7/072002

[32] S. Yu, 2019, NOVA-doc-39328-v1

[33] J. B. Birks, Proc. Phys. Soc. A **64**, 874 (1951), 10.1088/0370-1298/64/10/303

[34] I. Frank and I. Tamm, *Coherent Visible Radiation of Fast Electrons Passing Through Matter*, Springer Berlin Heidelberg (1991), ISBN 978-3-642-74626-0, pp. 29–35, 10.1007/978-3-642-74626-0_2

[35] M. Dolce and M. Martinez-Casales, 2020, NOVA-doc-45359-v7

[36] J. Huang, M. Judah, and D. Pershey, 2019, NOVA-doc-27689-v5

[37] M. Baird *et al.*, J. Phys. Conf. Ser. **664**, 072035 (2015), 10.1088/1742-6596/664/7/072035

[38] A. Rodriguez and A. Laio, Science **344**, 1492 (2014), 10.1126/science.1242072

[39] M. Baird, 2012, NOVA-doc-8241-v1

[40] M. Messier, 2012, NOVA-doc-7530-v4

[41] E. Niner, 2012, NOVA-doc-7648-v2

[42] R. E. Kalman, J. Basic Eng. **82**, 35 (1960), 10.1115/1.3662552

[43] N. Raddatz, 2015, NOVA-doc-13545-v1

[44] T. Alion and M. Campbell, 2017, NOVA-doc-13579-v35

[45] A. Himmel, A. Moren, and E. Niner, 2020, NOVA-doc-42766-v2

[46] B. Mayes and A. T. C. Sutton, 2019, NOVA-doc-42268-v1

[47] R. Gandrajula and L. Kolupaeva, 2019, NOVA-doc-42473-v1

[48] T. Warburton, 2019, NOVA-doc-42358-v2

[49] J. Porter, 2019, NOVA-doc-42277-v1

[50] M. Groh and T. Warburton, 2020, NOVA-doc-42897-v2

[51] A. Aurisano *et al.*, JINST **11**, P09001 (2016), arXiv:1604.01444 [hep-ex]

[52] F. Psihas *et al.*, Phys. Rev. D **100**, 073005 (2019), arXiv:1906.00713 [physics.ins-det]

[53] M. Groh, 2020, NOVA-doc-43911-v5

[54] J. Hewes and O. Samoylov, 2020, NOVA-doc-43935-v3

[55] M. Baird *et al.*, 2020, NOVA-doc-43162-v3

[56] S. Lein, 2016, NOVA-doc-15211-v1

[57] M. Wei, 2020, NOVA-doc-43757-v1

[58] S. Yu, 2020, NOVA-doc-43814-v3

[59] E. Catano-Mur, B. N. Nayak, A. T. C. Sutton, and T. Warburton, 2020, NOVA-doc-44040-v1

[60] M. Baird and L. Vinton, 2017, NOVA-doc-23390-v2

[61] E. Smith, 2020, NOVA-doc-46355-v7

[62] E. Catano-Mur, 2017, NOVA-doc-23174-v2

[63] M. Elkins, 2020, NOVA-doc-43712-v3

[64] S. Yu, 2018, NOVA-doc-29612-v10

[65] A. Mislivec, 2020, NOVA-doc-44401-v5

[66] M. Elkins and L. Kolupaeva, 2020, NOVA-doc-44316-v2

[67] M. A. Acero *et al.* [NOvA], Phys. Rev. D **98**, 032012 (2018), arXiv:1806.00096 [hep-ex]

[68] C. Backhouse, 2013, NOVA-doc-9222-v4

[69] A. Mislivec and T. Nosek, 2020, NOVA-doc-44298-v3

[70] T. Nosek, 2020, NOVA-doc-45668-v3

[71] L. Aliaga, C. Beunneti, L. Cremonesi, K. Maan, and A. Radovic, 2017, NOVA-doc-17608-v5

[72] M. Strait, 2020, NOVA-doc-20816-v23

[73] J. Neyman, Philos. Trans. R. Soc. A **236**, 333 (1937), 10.1098/rsta.1937.0005

[74] M. Tanabashi *et al.* [Particle Data Group], Phys. Rev. D **98**, 030001 (2018), 10.1103/PhysRevD.98.030001

[75] A. T. C. Sutton, 2020, NOVA-doc-45809-v7

[76] A. M. Hall, 2020, NOVA-doc-45889-v7

[77] G. J. Feldman and R. D. Cousins, Phys. Rev. D **57**, 3873 (1998), 10.1103/PhysRevD.57.3873

[78] P. Adamson *et al.* [MINOS+], Phys. Rev. Lett. **125**, 131802 (2020), arXiv:2006.15208 [hep-ex]

[79] M. G. Aartsen *et al.* [IceCube], Phys. Rev. Lett. **120**, 071801 (2018), arXiv:1707.07081 [hep-ex]

[80] Y. Nakajima, Recent results and future prospects from Super- Kamiokande, 2020, 10.5281/zenodo.4134680

[81] A. T. C. Sutton, 2020, NOVA-doc-48345-v4

[82] S. Y. Calvez, 2020, NOVA-doc-46331-v1

List of publications

NOvA publications with direct contribution

M. A. Acero *et al.* [NOvA], Phys. Rev. Lett. **123**, 151803 (2019), arXiv:1906.04907 [hep-ex]

M. A. Acero *et al.* [NOvA], Phys. Rev. D **98**, 032012 (2018), arXiv:1806.00096 [hep-ex]

NOvA technical notes

T. Nosek, 3Flavor 2020 Systematic Uncertainties Summary, 2020, NOVA-doc-45962-v2

A. Mislivec, T. Nosek, 3Flavor Systematics 2020 with p_{T} Extrap, 2020, NOVA-doc-44298-v3

A. Mislivec, T. Nosek, 3Flavor Systematics 2020, 2020, NOVA-doc-43974-v6

T. Nosek, Genie Cross Section Systematics for the 2020 3Flavor Analysis Using PCA, 2020, NOVA-doc-44274-v3

T. Nosek, Michel Electron Tagging Systematic for 3Flavor Analysis 2020, 2020, NOVA-doc-44271-v7

T. Nosek, Comparisons of ND RHC Data of Epochs 7d+8b and Periods 4+6 and Data/MC Comparison of Epochs 7d+8b for 2019 $\nu_e + \bar{\nu}_e$ Analysis, 2019, NOvA-doc-36780-v3

T. Nosek, Michel Decomposition for FHC 2018 ν_e Analysis, 2018, NOvA-doc-27938-v5

T. Nosek, Acceptance Systematics for 2018 ν_e+$\bar{\nu}_e$ Analysis – ND Subcomponents and ND/FD Kinematics, 2018, NOvA-doc-27935-v5

T. Nosek, ND ν_e RHC Data and MC Stability for 2018 ν_e Appearance Analysis, 2018, NOvA-doc-26690-v2

T. Nosek, ND ν_e Data and MC Stability for 2017 ν_e Appearance Analysis, 2017, NOvA-doc-23102-v7

T. Nosek, ND Subcomponents / Kinematics Systematics for 2017 ν_e Appearance Analysis, 2017, NOvA-doc-22478-v7

Selected proceedings

T. Nosek (for NOvA), Systematic Uncertainties of the NOvA Neutrino Oscillation Analysis, in PoS ICHEP2020, 210 (2021), 10.22323/1.390.0210

T. Nosek (for NOvA), Results on Neutrino and Antineutrino Oscillations from the NOvA Experiment, in Ukr. J. Phys. **64**, 613 (2019), 10.15407/ujpe64.7.613

T. Nosek (for NOvA), NOvA Recent Results with Neutrino+Antineutrino Data, in New Trends in High-Energy Physics, Dubna, JINR, ISBN 978-5-9530-0509-8 (2019), arXiv:1905.09109 [hep-ex]

T. Nosek, Effects of Matter in Neutrino Oscillations and Determination of Neutrino Mass Hierarchy at Long-baseline Experiments, in WDS'16 Proceedings of Contributed Papers – Physics (eds. J. Šafránková and J. Pavlů), Prague, Matfyzpress (2016), arXiv:1612.09132 [hep-ph]